

# Inferring potential landslide damming using slope stability, geomorphic constraints and run-out analysis; case study from the NW Himalaya

Vipin Kumar<sup>1\*</sup>, Imlirenla Jamir<sup>2</sup>, Vikram Gupta<sup>3</sup>, Rajinder K. Bhasin<sup>4</sup>

<sup>1</sup>Georisks and Environment, Department of Geology, University of Liege, Liege, Belgium

<sup>2</sup>Public Works Department (PWD), Nagaland, India

<sup>3</sup>Wadia Institute of Himalayan Geology, Dehradun, India

<sup>4</sup>Norwegian Geotechnical Institute, Oslo, Norway

\*Correspondence: [v.chauhan777@gmail.com](mailto:v.chauhan777@gmail.com); B-18, B-4000, Sart-Tilman, Liege, Belgium

## 1 ABSTRACT

2 Prediction of potential landslide damming has been a difficult process owing to the  
3 uncertainties related to ~~the~~ landslide volume, resultant dam volume, entrainment, valley  
4 configuration, river discharge, material composition, friction, and turbulence associated with  
5 material. In this study, instability pattern of landslides, geomorphic indices, post failure run-  
6 out predictions, and spatio-temporal **pattern** of rainfall and **earthquake** are explored to predict  
7 the potential landslide damming sites. The Satluj valley, NW Himalaya is chosen as a case  
8 study area. The study area has witnessed landslide damming in the past and incurred **\$ ~30M**  
9 **loss** and 350 lives in the last four decades due to such processes. Forty-four active landslides  
10 that cover a total  $\sim 4.81 \pm 0.05 \times 10^6 \text{ m}^2$  area and  $\sim 34.1 \pm 9.2 \times 10^6 \text{ m}^3$  volume are evaluated to  
11 identify those landslides that may result in ~~the~~ potential landslide damming. Out of forty-four,  
12 five landslides covering a total volume of  $\sim 26.3 \pm 6.7 \times 10^6 \text{ m}^3$  are noted to form the potential  
13 landslide dams. Spatio-temporal **varying** pattern of ~~the~~ rainfall in the recent years enhanced the  
14 possibility of landslide triggering and hence of ~~the~~ potential damming. These five landslides  
15 also revealed  $24.8 \pm 2.7\text{m}$  to  $39.8 \pm 4.0\text{m}$  high debris **flow** in the run-out predictions.

16 **Key words:** Landslide damming, Slope stability; Run-out; Himalaya

## 17 1.0 INTRODUCTION

18 Landslide damming is a normal geomorphic process in ~~the~~ narrow river valleys and ~~has been~~  
19 ~~one of the most disastrous natural processes~~ (Dai et al. 2005; Gupta and Sah 2008; Delaney  
20 and Evans 2015; Fan et al. 2020). ~~There have been many studies that~~ explored ~~the~~ damming  
21 characteristics (Li et al. 1986; Costa and Schuster 1988; Takahashi and Nakawaga 1993;  
22 Ermini and Casagli 2003; Fujisawa et al. 2009; Stefanelli et al. 2016; Kumar et al. 2019a).  
23 However, studies concerning the prediction of potential landslide dams and their stability at  
24 regional scale have been relatively rare, particularly in Himalaya despite a history of landslide  
25 damming and flash floods (Gupta and Sah 2008; Ruiz-Villanueva et al. 2016; Kumar et al.  
26 2019a). In order to identify the landslides that have potential to form dams, following factors  
27 have been main requisites; (i) pre- and post-failure behaviour of landslide slopes, (ii) landslide  
28 volume, stream power, and morphological setting of the valley (Kumar et al. 2019a).

29 To understand the pre-failure pattern, ~~the~~ Finite Element Method (FEM) based slope stability  
30 evaluation has been among the most widely used approaches for ~~the~~ complex slope geometry  
31 (Griffiths and Lane 1999; Jing 2003; Jamir et al. 2017; Kumar et al. 2018). However, the  
32 selection of input parameters in ~~the~~ FEM analysis and set of assumptions (a material model,  
33 failure criteria, and convergence) may also result in ~~the~~ uncertainty in the final output (Wong  
34 1984; Cho 2007; Li et al. 2016). ~~Input parameters based uncertainty~~ can be resolved by  
35 performing ~~the~~ parametric analysis, whereas the utilization of most appropriate criteria can  
36 minimize the uncertainty caused by assumptions. Post-failure behavior of landslides can be  
37 understood using ~~the~~ run-out analysis (Hungr et al. 1984; Hutter et al. 1994; Rickenmann and  
38 Scheidl 2013). These methods could be classified into empirical/statistical and dynamical  
39 categories (Rickenmann 2005). Owing to the flexibility in rheology, solution approach,  
40 reference frame, and entrainment, dynamic models have been relatively more realistic for ~~the~~  
41 site-specific problems (Corominas and Mavrouli 2011). Though the different numerical models  
42 have different advantages and limitations, Voellmy rheology (friction and turbulence)  
43 (Voellmy 1955; Salm 1993) based Rapid Mass Movement Simulation (RAMMS) (Christen et  
44 al. 2010) ~~model~~ has been used widely owing to the inclusion of rheological and entrainment  
45 rate flexibility.

46 Apart from the pre and post-failure pattern, landslide volume, stream power and morphological  
47 setting of the valley are crucial to infer the potential landslide damming. Morphological  
48 Obstruction Index (MOI) and Hydro-morphological Dam Stability Index (HDSI) have been

49 widely used geomorphic indices to infer the potential of landslide dam formation and their  
50 temporal stability (Costa and Schuster 1988; Ermini and Casagli 2003; Stefanelli et al. 2016).

51 The NW Himalaya has been one of most affected terrains by the landslides owing to the active  
52 tectonics and multiple precipitation sources i.e., Indian Summer Monsoon (ISM) and Western  
53 Disturbance (Dimri et al. 2015). The NW Himalaya has ~~also~~ accommodated ~51 % of all the  
54 landslides in India during yrs. 1800-2011 (Parkash 2011). The Satluj River valley, NW  
55 Himalaya is one such region ~~that has~~ claimed ~350 lives and ~~loss of~~ minimum 30 million USD  
56 ~~due to the landslides and associated floods~~ in the last four decades ~~and~~ holds a high potential  
57 for ~~landslide~~ damming and resultant floods (Ruiz-Villanueva et al. 2016; Kumar et al.  
58 2019a). Therefore, ~~Satluj~~ valley is taken as a case study area, ~~of which~~ 44 active landslides  
59 belonging to the different litho-tectonic regimes are modeled using the FEM  
60 technique. Multiple slope sections and a range of values of different input parameters are used  
61 to perform the parametric study. In order to determine the human population that might be  
62 affected by these landslides, census statistics are also used. The MOI and HDSI are used to  
63 determine the potential of landslide dam formation and their stability, respectively. In view of  
64 the role of rainfall and earthquake ~~as~~ main landslide triggering factors, ~~spatio-temporal~~ regime  
65 of these two factors is also discussed. Run-out prediction of certain landslides is also performed  
66 to understand the role of run-out in the potential landslide damming. This study provides ~~a~~  
67 detailed insight into the regional instability pattern, associated uncertainty, and potential  
68 landslide damming sites and hence it can be replicated in other hilly terrain witnessing frequent  
69 landslides and damming.

## 70 **2.0 STUDY AREA**

71 The study area is located between the Moorang (31°36'1" N, 78°26' 47" E) and Rampur town  
72 (31°27'10" N, 77°38' 20" E) in the Satluj River valley, NW Himalaya (Fig. 1). The Satluj River  
73 flows across the Tethyan Sequence (TS), Higher Himalaya Crystalline (HHC), Lesser  
74 Himalaya Crystalline (LHC), and Lesser Himalaya Sequence (LHS). The TS in the study area  
75 comprises slate/phyllite and schist and has been intruded by the biotite-rich granite i.e.,  
76 Kinnaur-Kailash Granite (KKG) near the Sangla Detachment (SD) fault (Sharma 1977; Vannay  
77 et al. 2004). The SD fault separates the TS from the underlying crystalline rockmass of the  
78 HHC. Migmatitic gneiss marks the upper part of the HHC, whereas the base is marked by the  
79 kyanite-sillimanite gneiss rockmass (Sharma 1977; Vannay et al. 2004; Kumar et al. 2019b).  
80 The Main Central Thrust (MCT) fault separates the HHC from the underlying schist/gneissic

81 rockmass of the LHC. The LHC comprises mica schist, carbonaceous schist, quartzite, and  
82 amphibolite. A thick zone of gneiss i.e., Wangtu Gneissic Complex (WGC) is exposed in the  
83 LHC, which comprises augen gneiss and porphyritic granitoids. The LHC is delimited at the  
84 base by the Munsiri Thrust (MT) fault that is thrust over the Lesser Himalaya Sequence  
85 (LHS) rockmass. The MT contains breccia, cataclastic, and fault gouge (Sharma 1977; Vannay  
86 et al. 2004; Kumar et al. 2019b). The LHS in the study area consists of quartz-arenite (Rampur  
87 Quartzite) with bands of phyllite, meta-volcanics, and paragneiss (Sharma 1977).

88 The present study covers forty-four active landslides (20 debris slides, 13 rock falls, and 11  
89 rock avalanches) along the study area (Table 1) that have been mapped recently by Kumar et  
90 al. (2019b). Field photographs of some of these landslides are presented in Fig. 2. The TS and  
91 LHS in the study area have been subjected to the tectonic tranquility with exhumation rates as  
92 low as 0.5 - 1.0 mm/yr, whereas the HHC and LHC region comprise 1.0 - 4.5 mm/yr rate of  
93 exhumation (Thiede et al. 2009). The MCT fault region and the WGC are noted to have  
94 maximum exhumation rate (i.e., ~4.5 mm/yr) that is evident from the deep gorges in these  
95 regions (Fig. 2c, 2e). Further, a majority of the earthquake events in the study area in the last 7  
96 decades have been related to the N-S oriented Kaurik - Chango Fault (KCF) (Kundu et al. 2014;  
97 Hazarika et al. 2017; International Seismological Centre Catalogue 2019). The climate zones  
98 in the study area shows a spatial variation from the humid (~800 mm/yr) in the LHS to the  
99 semi-arid (~200 mm/yr) in the TS (Kumar et al. 2019b). The HHC acts as a transition zone  
100 where climate varies from semi-humid to semi-arid in the SW-NE direction. This transition has  
101 been attributed to the 'orographic barrier' nature of the HHC that marks the region in its north  
102 as 'orographic interior' and the region to its south as the 'orographic front' (Wulf et al. 2012;  
103 Kumar et al. 2019b).

104 The landslides in the study area have been a consistent threat to the socio-economic condition  
105 of the nearby human population (Gupta and Sah 2008; Ruiz-Villanueva et al. 2016; Kumar et  
106 al. 2019a). Therefore, the human population in the vicinity of each landslide was also  
107 determined by considering the villages/town in that region. It is to note that total 25,822 people  
108 reside in the 500 m extent of the 44 landslide slopes and about 70 % of this population is  
109 residing in the reach of debris slide type landslides. Since the Govt. of India follows a 10 year  
110 gap in census statistics, the human population data was based on last official i.e., Census-2011.  
111 The next official census is due in year 2021. The population density in the Indian Himalayan  
112 region was estimated to be 181/km<sup>2</sup> in the year 2011 that might grow to 212/km<sup>2</sup> in 2021 with

113 a decadal growth rate of 17.3% (<https://censusindia.gov.in>, retrieved on 02 Sep 2020;  
114 <http://gbpihedenvi.nic.in>, retrieved on 02 Sep 2020).

### 115 **3.0 METHODOLOGY**

116 The methodology involved ~~the~~ field data collection, satellite imagery analysis, laboratory  
117 analyses, slope stability modelling, geomorphic indices, rainfall/earthquake pattern and run-  
118 out modelling. Details are as follows;

#### 119 *3.1 Field data, satellite imagery processing, and laboratory analyses*

120 The field work involved rock/soil sample collection from each landslide location, rockmass  
121 joint mapping, and N-type Schmidt Hammer Rebound (SHR) measurement. ~~The~~ joints were  
122 included in the slope models for the FEM based slope stability analysis. ~~Dataset~~ involving the  
123 joint details is available in the data repository (Kumar et al. 2020). The SHR values were  
124 obtained as per International Society of Rock Mechanics (ISRM) standard (Aydin 2008). ~~The~~  
125 Cartosat-1 satellite imagery and field assessment were used to finalize the location of slope  
126 sections (2D) of the landslides. ~~The~~ Cartosat-1 imagery has been used widely for the landslide  
127 related studies (Martha et al. 2010). The Cartosat-1 Digital Elevation Model (DEM), prepared  
128 using the Cartosat-1 stereo imagery, was used to extract the slope sections of the landslides  
129 using the Arc GIS-10.2 software. Details of the satellite imagery are mentioned in Table 2.

130 The rock/soil samples were analyzed in the National Geotechnical Facility (NGF) and Wadia  
131 Institute of Himalayan Geology (WIHG) laboratory, India. The rock samples were drilled and  
132 smoothed for Unconfined Compressive Strength (UCS) (IS: 9143-1979) and ultrasonic test  
133 (CATS Ultrasonic (1.95) of Geotechnical Consulting & Testing Systems). ~~The~~ Ultrasonic test  
134 was conducted to determine the density, elastic modulus, and Poisson's ratio of rock samples.  
135 The soil samples were tested for grain size analysis (IS: 2720-Part 4-1985), UCS test (IS: 2720-  
136 Part 10-1991), and direct shear test (IS: 2720-Part 13- 1986). If the soil samples contained <  
137 5% fines (< 75 mm), hydrometer test was not performed for the remaining fine material. In the  
138 direct shear test, soil samples were sheared under the constant normal stress of 50, 100 and 150  
139 kN/m<sup>2</sup>. The UCS test of soil was performed under three different rates of movements i.e., 1.25  
140 mm/min, 1.50 mm/min and 2.5 mm/min.

#### 141 *3. 2 Slope stability modelling*

142 The Finite Element Method (FEM) was used along with the Shear Strength Reduction (SSR)

143 technique to infer the critical Strength Reduction Factor (SRF), Shear Strain (SS), and Total  
144 Displacement (TD) in the 44 landslide slopes using the RS2 software. The SRF has been  
145 observed to be similar in nature as the Factor of Safety (FS) of the slope (Zienkiewicz et al.  
146 1975; Griffiths and Lane 1999). To define the failure in the SSR approach, non-convergence  
147 criteria was used (Nian et al. 2011). The boundary condition with the restraining movement  
148 was applied to the base and back, whereas the front face was kept free for the movement (Fig.  
149 3). In-situ field stress was adjusted in view of dominant stress i.e., extension or compression,  
150 by changing the value of the coefficient of earth pressure (k). The  $k = \sigma_h/\sigma_v = 0.5$  was used in  
151 extensional regime, whereas  $k = \sigma_h/\sigma_v = 1.5$  was used in compressional regime. The Tethyan  
152 Sequence has been observed to possess the NW-SE directed extensional regime. The structures  
153 in the upper part of the HHC are influenced by the east directed extension along the SD fault.  
154 The lower part, however, ~~comprises the signs of~~ the SW directed compression along the Main  
155 Central Thrust. In contrast to the HHC, structures in the Lesser Himalaya Crystalline and  
156 Munsiri Thrust region are influenced by the compressional regime. In the Lesser Himalaya  
157 Sequence region, the SW directed compressional regime has been observed on the basis of the  
158 SW verging folds, crenulation cleavage, and other features (Vannay et al. 2004).

159 The soil and rock mass were used in the models through the Mohr-Coulomb (M-C) failure  
160 criterion (Coulomb 1776; Mohr 1914) and Generalized Hoek-Brown (GHB) criterion (Hoek et  
161 al. 1995), respectively. The parallel- statistical distribution of the joints with normal-  
162 distribution joint spacing in the rock mass was applied through the Barton-Bandis (B-B) slip  
163 criterion (Barton and Choubey 1977; Barton and Bandis 1990). Plane strain triangular elements  
164 having 6 nodes were used through the graded mesh in the models. Details of the criteria used  
165 in the FEM analysis are mentioned in Table 3. ~~Dataset involving the value~~ of input parameters  
166 used in the FEM analysis is available in the data repository (Kumar et al. 2020). It is to note  
167 that the FEM analysis is performed under the static load i.e., field stress and body force. The  
168 dynamic analysis is not performed, at present, in absence of any major seismic events in the  
169 region in the last 4 decades (sec. 4.3) and lack of reliable dynamic load data of nearby major  
170 seismic events.

171 To understand the uncertainty caused by the selection of 2D slope section, multiple slope  
172 sections were taken, wherever possible. More than one slope sections were modeled for each  
173 debris slide, whereas for the rock falls/ rock avalanche only one slope section was chosen due  
174 to the limited width of the rock falls/rock avalanche in the study area. To find out the relative  
175 influence of different input parameters on the final output, a parametric study was performed.

176 In the parametric study for debris slides, Akpa landslide (S.N.5 in Fig. 3), Pangi landslide  
 177 (S.N.13 in Fig. 3), and Barauni Gad landslide (S.N.38 in Fig. 3) were chosen, whereas Tirung  
 178 khad (S.N.2 in Fig.3) and Chagaon landslide (S.N.21 in Fig. 3) were considered to represent  
 179 rock fall. Baren Dogri (S.N.7 in Fig. 3) landslide was used to represent the rock avalanches.  
 180 The selection of these landslides for the parametric study was based on the following two  
 181 factors; (1) to choose the landslides from different litho-tectonic regime, (2) representation of  
 182 varying stress regime i.e., extensional, compressional, and relatively stagnant. The Parametric  
 183 study of the debris slide models involved following 9 parameters; field stress coefficient,  
 184 stiffness ratio, cohesion and angle of friction of soil, elastic modulus and Poisson's ratio of soil,  
 185 rockmass modulus, Poisson's ratio and uniaxial compressive strength of rock. For the  
 186 rockfalls/rock avalanche, following 6 parameters; uniaxial compressive strength of rock,  
 187 rockmass modulus of rock, Poisson's ratio of rock, 'mi' parameter, stiffness ratio, and field  
 188 stress coefficient were used. The 'mi' is a Generalized Hoek-Brown (GHB) parameter that is  
 189 equivalent to the angle of friction of Mohr-coulomb (M-C) criteria.

### 190 3. 3 Geomorphic indices

191 Considering the possibility of landslide dam formation in case of slope failure, following  
 192 geomorphic indices are also used;

193 (i) Morphological Obstruction Index (MOI)

$$194 \quad \text{MOI} = \log (V_l/W_v) \quad \text{Eq. 1}$$

195 (ii) Hydro-morphological Dam Stability Index (HDSI)

$$196 \quad \text{HDSI} = \log (V_d/A_b.S) \quad \text{Eq. 2}$$

197 Where,  $V_d$  (dam volume) =  $V_l$  (landslide volume),  $m^3$ ;  $A_b$  is upstream catchment area ( $km^2$ );  $W_v$   
 198 is width of the valley (m) and  $S$  is local slope gradient of river channel (m/m). Though the  
 199 resultant dam volume could be higher or lower than the landslide volume owing to the slope  
 200 entrainment, rockmass fragmentation, retaining of material at the slope, and washout by the  
 201 river (Hungry and Evans 2004; Dong et al. 2011), dam volume is assumed to be equal to  
 202 landslide volume for the worst case. By utilizing the comprehensive dataset of ~300 landslide  
 203 dams of Italy, Stefanelli et al. (2016) have classified the MOI into (i) non-formation domain:  
 204  $MOI < 3.00$ , (ii) uncertain evolution domain:  $3.00 < MOI < 4.60$  and (iii) formation domain:  $MOI$

205 >4.60. By utilizing the same dataset, Stefanelli et al. (2016) defined the HDSI into following  
206 categories (i) instability domain:  $HDSI < 5.74$ , (ii) uncertain determination domain:  $5.74 < HDSI$   
207  $> 7.44$ , and (iii) Stability domain:  $HDSI > 7.44$ .

### 208 3. 4 Rainfall and Earthquake regime

209 Precipitation in the study area ~~owes its existence~~ to the Indian Summer Monsoon (ISM) and  
210 Western Disturbance (WD) and varies spatially-temporally due to various local and regional  
211 factors (Gadgil et al. 2007; Hunt et al. 2018). Therefore, we have taken the **TRMM\_3B42** daily  
212 rainfall data of years 2000-2019 at four different locations; Moorang, Kalpa, Nachar, and  
213 Rampur (Locations mentioned in Fig. 1). The dataset of earthquake events ( $2 < M < 8$ ) in and  
214 around study area during the years 1940-2019 was retrieved from the ISC catalogue  
215 (<http://www.isc.ac.uk/iscbulletin/search/catalogue/>, retrieved on 02 March 2020) to determine  
216 the spatio-temporal pattern.

### 217 3. 5 Run-out modelling

218 Since the study area has witnessed many disastrous landslides, mostly rainfall triggered, and  
219 flash floods in past (Gupta and Sah 2008; Ruiz-Villanueva et al. 2016), run-out analysis was  
220 performed to understand the post-failure scenario. Such run-out predictions will also be helpful  
221 to ascertain the possibility of damming because various studies have noted ~~the river damming~~  
222 by the debris flows (Li et al. 2011; Braun et al. 2018; Fan et al. 2020). ~~Therefore, the~~ landslides  
223 that have potential to form ~~the~~ dams based on the indices (sec. 3.3) are evaluated for such run-  
224 out analysis.

225 In this study, Voellmy rheology (Voellmy 1955; Salm 1993) based Rapid Mass Movement  
226 Simulation (RAMMS) (Christen et al. 2010) model is used to understand the run-out pattern.  
227 The RAMMS for debris flow uses the Voellmy friction law and divides the frictional resistance  
228 into a dry-Coulomb type friction ( $\mu$ ) and viscous-turbulent friction ( $\xi$ ). The frictional resistance  
229  $S$  (Pa) is thus;

$$230 \quad S = \mu N + (\rho g u^2) / \xi \quad \text{Eq. 3}$$

231 where  **$N; \rho h g \cos(\phi)$**  is the normal stress on the running surface,  $\rho$  density,  $g$  gravitational  
232 acceleration,  $\phi$  slope angle,  $h$  flow height and  $u = (u_x, u_y)$ , consisting of the flow velocity in  
233 the x- and y-directions. In this study, a range of friction ( $\mu$ ) and turbulence ( $\xi$ ) values, apart  
234 from other input parameters, are used to ~~eliminate~~ the uncertainty in output (Table 4).

235 Generally, the values for  $\mu$  and  $\xi$  parameters are achieved using the reconstruction of real events  
236 through the simulation and subsequent comparison between the dimensional characteristics of  
237 real and simulated event. However, the landslides in the study area merge with the river floor  
238 and/or are in close proximity and hence there is no failed material left from the previous events  
239 to reconstruct. Therefore, the  $\mu$  and  $\xi$  values were taken in a range in view of topography of  
240 landslide slope and run-out path, landslide material, similar landslide events/material, and  
241 based on previous studies/models (Hurlimann et al. 2008; Rickenmann and Scheidl 2013;  
242 RAMMS v.1.7.0). Since these landslides are relatively deep in nature and we are of  
243 understanding that during the slope failure, irrespective of type of trigger, entire loose material  
244 might not slide down, the depth of landslide is taken as only  $\frac{1}{4}$  (thickness) in the run-out  
245 calculation. Further, a release area concept (for unchanneled flow or block release) was used  
246 for the run-out simulation. During the field visits, no specific flow channels (or gullies) were  
247 found on the landslide slopes except a few centimeters deep seasonal flow channels for S. N.  
248 5 and S.N. 15 landslides (Table 1). However, the data pertaining to the spatial-temporal  
249 information of discharge at these two landslides was not available. Therefore, the release area  
250 concept was chosen because it has been more appropriate when the flow path (e.g. gully) and  
251 its possible discharge on the slope is uncertain (RAMMS v.1.7.0).

## 252 4.0 RESULTS

### 253 4.1 Slope instability regime and parametric output

254 Results indicated that out of 44 landslides, 31 are in meta-stable state ( $1 \leq FS \leq 2$ ) and 13 in  
255 unstable state ( $FS < 1$ ) (Fig. 4). Most of the unstable landslides are debris slides, whereas the  
256 majority of the meta-stable landslides are rock fall/rock avalanche. Debris slides constitute ~  
257 90 % and ~99 % of the total area and volume, respectively of the unstable landslides. It is to  
258 note that about ~70 % of the total human population along the study area resides in the vicinity  
259 (~500 m) of these unstable debris slides (Fig. 4). Rock falls/Rock avalanches constitute ~84 %  
260 and ~78 % of the area and volume, respectively of the meta-stable landslides. Out of total 20  
261 debris slides, 12 debris slides are found to be in unstable stage, whereas 8 in the meta-stable  
262 condition (Fig. 4). These 20 debris slides occupy  $\sim 1.9 \pm 0.02 \times 10^6 \text{ m}^2$  area and  $\sim 26 \pm 6 \times 10^6$   
263  $\text{m}^3$  volume. While comparing the Factor of Safety (FS) with the Total Displacement (TD) and  
264 Shear Strain (SS), nonlinear poor correlation is achieved (Fig. 5). Since, the TD and SS present  
265 a relatively good correlation (Fig. 5), only the TD is used further along with the FS. The TD  
266 ranges from  $7.4 \pm 8.9 \text{ cm}$  to  $95.5 \pm 10 \text{ cm}$  for the unstable debris slides and  $\sim 18.8 \text{ cm}$  for meta-

267 stable landslides (Fig. 4). Out of 13 rockfalls, 1 belongs to the unstable state and 12 to the meta-  
268 stable state (Fig. 4). The TD varies from 0.4 to 80 cm with the maximum for Bara Kamba  
269 rockfall (S.N. 31). Out of 11 rock avalanches, 1 belongs to the unstable state and 10 to the  
270 meta-stable state (Fig. 4). The TD varies from 6.0 to 132.0 cm with the maximum for the  
271 Kandar rock avalanche (S.N. 25). Relatively higher TD is obtained by the rock fall and rock  
272 avalanche of the Lesser Himalaya Crystalline region (Fig. 4). The landslides of the Higher  
273 Himalaya Crystalline (HHC), Kinnaur Kailash Granite (KKG) and Tethyan Sequence (TS),  
274 despite being only 17 out of the total 44 landslides, constituted ~ 67 % and ~ 82 % of the total  
275 area and total volume of the landslides.

276 The Factor of Safety (FS) of debris slides is found to be relatively less sensitive to the change  
277 in the value of input parameters than the Total Displacement (TD) (Fig. 6). In case of Akpa  
278 (Fig. 6a) and Pangi landslide (Fig. 6b), soil friction and field stress have more influence on the  
279 FS. However, for ~~the~~ TD, field stress, elastic modulus and Poisson's ratio of the soil are  
280 relatively more controlling parameters. The FS and TD of the Barauni Gad landslide (Fig. 6c)  
281 are relatively more sensitive to soil cohesion and 'mi' parameter. Therefore, it can be inferred  
282 that the FS of debris slides is more sensitive to soil friction and field stress, whereas TD is  
283 mostly controlled by the field stress and deformation parameters i.e, elastic modulus and  
284 Poisson's ratio. Similar to the debris slides, the FS of rock falls and rock avalanche are found  
285 to be relatively less sensitive than TD to the change in the value of input parameters (Fig. 7).  
286 Tirung Khad rock fall (Fig. 7a) and Baren Dogri rock avalanche (Fig. 7b) show dominance of  
287 'mi' parameter and field stress in the FS as well as in TD. In case of Chagaon rock fall (Fig.  
288 7c), Poisson's ratio and UCS have relatively more influence on FS and TD. Thus, it can be  
289 inferred that the rock fall/rock avalanche are more sensitive to 'mi' parameter and field stress.

#### 290 *4.2 Potential landslide damming*

291 Based on the MOI, out of total 44 landslides, 5 (S.N. 5, 7, 14, 15, 19) are observed to be in the  
292 formation domain, 15 in uncertain domain, and 24 in non-formation domain (Fig. 8a). ~~These~~  
293 five landslides that have potential to dam the river in case of slope failure ~~accommodate~~  $\sim 26.3$   
294  $\pm 6.7 \times 10^6 \text{ m}^3$  volume (Fig. 9 a-e). In terms of temporal stability (or durability), out of these  
295 five landslides, only one landslide (S.N. 5) is noted to attain the 'uncertain' domain, whereas  
296 the remaining four show 'instability' (Fig. 8b,d). The lacustrine deposit in the upstream of  
297 Akpa landslide (S.N. 5) in Fig. 9a ~~implies the~~ signs of landslide damming in the past ~~also~~ (Fig.  
298 10). The 'uncertain' temporal stability indicates that the landslide dam may be stable or

299 unstable depending upon the stream power and landslide volume, which in turn are dynamic  
300 factors and may change owing to the changing climate and/or tectonic event. The landslides  
301 that have been observed to form the landslide dam but are noted to be in temporally unstable  
302 category (S.N. 7, 14, 15, 19) are still considerable owing to the associated risks of lake-  
303 impoundment and generation of secondary landslides. Urni landslide (S.N. 19) (Fig. 9e) that  
304 damaged the part of National Highway road (NH)-05 has already partially dammed the river  
305 since year 2016 and holds potential for the further damming (Kumar et al. 2019a). Apart from  
306 the S.N. 5 and S.N. 19 landslides, remaining landslides (S.N. 7, 14, 15) belong to the Higher  
307 Himalaya Crystalline (HHC) region that has been observed to accommodate many landslide  
308 damming and subsequent flash floods events in the geological past (Sharma et al. 2017).

#### 309 *4.3 Rainfall and Earthquake regime*

310 In order to explain the spatio-temporal variation in the rainfall, topographic profile of the study  
311 area is also plotted along with the rainfall variation (Fig. 11a). The temporal distribution of  
312 rainfall is presented at annual, monsoonal i.e., Indian Summer Monsoon (ISM): June-  
313 September and non-monsoonal i.e., Western Disturbance (WD): Oct-May (Fig. 11b-d) level.  
314 Rainfall data of the years 2000-2019 revealed a relative increase in the annual rainfall since the  
315 year 2010 (Fig. 11b). The Kalpa region (orographic barrier) received a relatively more annual  
316 rainfall than the Rampur, Nachar and Moorang region throughout the time period, except the  
317 year 2017. The rainfall dominance at Kalpa is more visible in non-monsoonal season (Fig.  
318 11d). It may be due to its orographic influence on the saturated winds of the WD (Dimri et al.  
319 2015). Further, the rainfall during the monsoon season that was dominant at the Rampur region  
320 till year 2012 gained dominance at Kalpa region since the year 2013 (Fig. 11c).

321 Extreme rainfall events of June 2013 that resulted in the widespread slope failure in the NW  
322 Himalaya also caused landslide damming at places (National Disaster Management Authority,  
323 Govt. of India, 2013; Kumar et al. 2019a). Similar to the year 2013, the year 2007, 2010 and  
324 2019 also witnessed enhanced annual rainfall and associated flash floods and/or landslides in  
325 the region (hpervis.nic.in, retrieved on March 1, 2020; sandrp.in, retrieved on March 1, 2020).  
326 However, the contribution of the ISM and WD associated rainfall has been variable in these  
327 years (Fig. 11). Such frequent but inconsistent rainfall events that possess varied (temporally)  
328 dominance of the ISM and WD are noted to owe their occurrence to the following local and  
329 regional factors; El-Nino Southern Oscillation (ENSO), Equatorial Indian Ocean Circulation  
330 (EIOC), and planetary warming (Gadgil et al. 2007; Hunt et al. 2018). The orographic setting

331 is noted to act as a main local factor as evident from the relatively more rainfall (total  
332 precipitation=1748±594 mm/yr.) at Kalpa region (orographic barrier) in the non-monsoon and  
333 monsoon season from the year 2010 onwards (Fig. 11). Prediction of the potential landslide  
334 damming sites in the region revealed that four (S.N. 7, 14, 15, 19) out of five landslides that  
335 ~~can form the dam~~ belong to this orographic barrier region. Therefore, in view of the prevailing  
336 rainfall trend since the year 2010, regional factors, discussed above, and orographic setting,  
337 precipitation triggered slope failure events ~~cannot be denied~~ in the future. Such slope failure  
338 events, if ~~occurred~~, at the predicted landslide damming sites may certainly dam the river.

339 The seismic pattern revealed that the region has been hit by 1662 events during the years 1940-  
340 2019 with the epicenters located in and around the study area (Fig. 12a). However, ~99.5 % of  
341 these earthquake events had a magnitude of less than 6.0 and only 8 events are recorded in the  
342 range of 6.0 to 6.8  $M_s$  (International Seismological Centre 2019). Out of these 8 events, only  
343 one event i.e., 6.8  $M_s$  (19<sup>th</sup> Jan. 1975) has been noted to induce ~~the~~ widespread slope failures  
344 in the study area (Khattari et al. 1978). The majority of the earthquake events in the study area  
345 ~~has~~ occurred in the vicinity of the N-S oriented trans-tensional Kaurik - Chango Fault (KCF)  
346 that accommodated the epicenter of 19<sup>th</sup> Jan. 1975 earthquake (Hazarika et al. 2017;  
347 <http://www.isc.ac.uk/iscbulletin/search/catalogue/>, retrieved on 02 March 2020). About 95%  
348 of the total 1662 events had their focal depth within 40 km (Fig. 12b). Such a relatively low  
349 magnitude - shallow seismicity in the region has been related to the Main Himalayan Thrust  
350 (MHT) decollement as a response to the relatively low convergence ( $\sim 14\pm 2$  mm/yr) of India  
351 and Eurasia plates in the region (Bilham 2019) (Fig. 12c). Further, the arc (Himalaya)-  
352 perpendicular Delhi-Haridwar ridge that is under thrusting the Eurasian plate in this region has  
353 been observed to be responsible for the spatially varied *low* seismicity in the region (Hazarika  
354 et al. 2017). Thus, though the study area has been subjected to frequent earthquakes, chances  
355 of earthquake-triggered landslides have been relatively low in comparison to rainfall-triggered  
356 landslides and associated landslide damming. For this reason and the lack of reliable dynamic  
357 load of major earthquake event, we have performed the *static* modelling in the present study.  
358 However, we intend to perform the *dynamic* modelling in near future if the reliable dynamic  
359 load data will be available.

#### 360 4.4 Run-out analysis

361 All five landslides (S.N. 5, 7, 14, 15, 19 in Fig. 9) that are ~~observed~~ to form potential landslide  
362 ~~dam~~ in case of slope failure were also used for the run-out analysis. Results are as follows;

363 4.4.1 Akpa landslide (S.N. 5)

364 Though it is difficult to ascertain ~~that how much part of the~~ debris flow might contribute in the  
365 river blockage, it will certainly block the river in view of ~38 m high debris material with ~50  
366 m wide run-out across the channel in this narrow part of river valley (Fig. 9a) even at maximum  
367 value of coefficient of friction (i.e.,  $\mu = 0.3$ ) (Fig. 13a). ~~It is to note that~~ not only the run-out  
368 extent but flow height also decreases on increasing the friction value (Fig. 13a.1-13.a.3). The  
369 maximum friction ~~can take~~ into account the shear resistance by slope material and the bed-load  
370 on the river channel. However, apart from the frictional characteristics of run-out path,  
371 turbulence of debris flow also controls its dimension and hence consequences like potential  
372 damming. Therefore, different values of turbulence coefficient ( $\xi$ ) were used (Table 4). The  
373 resultant flow height (representing 9 sets of debris flow obtained using  $\mu = 0.05, 0.1$  and  $0.3$  and  
374  $\xi = 100, 200$  and  $300 \text{ m/s}^2$ ) attains its peak value i.e.,  $39.8 \pm 4.0 \text{ m}$  at the base of central part of  
375 landslide (Fig. 14a).

376 4.4.2 Baren dogri landslide (S.N. 7)

377 At the maximum friction value ( $\mu = 0.4$ ), Baren dogri landslide ~~is noted to~~ attain a peak value  
378 of flow height i.e., ~30 m at the base of central part of landslide (Fig. 13b). Similar to the valley  
379 configuration around the Akpa landslide (sec 4.4.1), river valley attains a narrow/deep gorge  
380 setting here also (Fig. 9b). The maximum value of debris flow height obtained using the  
381 different  $\mu$  and  $\xi$  values is  $25.6 \pm 2.1 \text{ m}$  (Fig. 14b). Flow material is also noted to attain more  
382 run-out in upstream direction of river (~1100 m) than in the downstream direction (~800 m).  
383 This spatial variability in the run-out length might exist due to the river channel configuration  
384 as river channel in upstream direction is relatively narrower than the downstream direction.

385 4.4.3 Pawari landslide (S.N. 14)

386 Pawari landslide attains maximum flow height of ~20 m at the maximum friction of run-out  
387 path ( $\mu = 0.4$ ) (Fig. 13c). The resultant debris flow that is achieved using the different values of  
388  $\mu$  and  $\xi$  parameters attains a peak value of  $24.8 \pm 2.7 \text{ m}$  and decreases gradually with a run-out  
389 of ~1500 m in upstream and downstream direction (Fig. 14c). This landslide resulted in the  
390 relatively long run-out of ~1500 in the upstream and downstream direction. Apart from the  
391 landslide volume that affects the run-out extent, valley morphology also controls it as evident  
392 from the previous landslides. The river channel in upstream and downstream direction from  
393 the landslide location is observed to be narrow (Fig. 9c).

394 4.4.4 Telangi landslide (S.N. 15)

395 Telangi landslide is noted to result in peak debris flow height of ~24 m at the maximum friction  
396 ( $\mu=0.4$ ) (Fig. 13d). It is to note that on increasing the friction of run-out path, flow run-out  
397 decreased along the river channel but increased across the river channel resulting into possible  
398 damming. The debris flow after taking into account different values of  $\mu$  and  $\xi$  parameters  
399 attains a peak value of  $25.0 \pm 4.0$  m (Fig. 14d). Similar to Baren dogri landslide (S.N. 7),  
400 material attained more run-out in upstream direction of river (~1800 m) than in downstream  
401 direction (~600 m) that attributes to narrower river channel in upstream than the downstream  
402 direction. The downstream side attains wider river channel due to the traversing of Main  
403 Central Thrust (MCT) fault in the proximity (Fig. 1). Since Pawari and Telangi landslide (S.N.  
404 14 & 15) are situated ~500 m from each other, their respective flow run-outs might mix in the  
405 river channel resulting into disastrous cumulative effect.

406 4.4.5 Urni landslide (S.N. 19)

407 Urni landslide attained a peak value of ~44 m of debris flow height at the maximum friction  
408 value ( $\mu=0.4$ ) (Fig. 13e). After taking into account different values of  $\mu$  and  $\xi$  parameters, the  
409 debris flow attained a height of  $26.3 \pm 1.8$  m (Fig. 14e). Relatively wider river channel in  
410 downstream direction (Fig. 9e) is considered to results in long run-out in downstream direction  
411 than in the upstream.

412 **5.0 DISCUSSION**

413 Present study aimed to determine the potential landslide damming sites in the Satluj River  
414 valley, NW Himalaya. In order to achieve this objective, 44 landslides were considered. At  
415 first, slope stability evaluation of all the slopes was performed alongwith the parametric  
416 evaluation. Then the geomorphic indices i.e., Morphological Obstruction Index (MOI) and  
417 Hydro-morphological Dam Stability Index (HDSI) were used to predict the formation of  
418 potential landslide dam and their subsequent stability. Rainfall and earthquake regime were  
419 also explored in the study area. Finally, run-out analysis was performed of those landslides that  
420 have been observed to form the potential landslide dam.

421 The MOI revealed that out of 44 landslides, five (S.N. 5, 7, 14, 15, 19) have potential to form  
422 the landslide dam (Fig. 8, 9). On evaluating the stability of such potential dam sites using the  
423 HDSI, the landslide (S.N. 5) is noted to attain an 'uncertain' domain ( $5.74 < \text{HDSI} < 7.44$ ) in

424 terms of dam stability. The uncertain term implies that the resultant dam may be stable or  
425 unstable depending upon the landslide/dam volume, upstream catchment area (or water  
426 discharge) and slope gradient (sec 3.3). Since this landslide (S.N.5) presents clear signs of  
427 having already formed a dam in the past, as indicated by the alternating fine-coarse layered  
428 sediment deposit (or lake deposit) in the upstream region (Fig. 10), recurrence ~~can't be denied.~~  
429 Further, run-out analysis of landslide has predicted  $39.8 \pm 4.0$ m high debris flow in the event of  
430 failure that will block the river completely (Fig. 13a, 14a). However, the durability of the  
431 blocking ~~can't be~~ ascertained as ~~it is subjected to~~ the volume of landslide that will be retained  
432 ~~at~~ the channel and river discharge.

433 Remaining four landslides (S.N. 7, 14, 15, 19), though ~~showed~~ instability i.e., HDSI  $< 5.74$  at  
434 present, may form ~~the dam~~ in near future as the region accommodating these landslides has  
435 been affected by such damming and subsequent flash floods in the past (Sharma et al. 2017).  
436 The last one of these i.e., S.N. 19 (Urni landslide) has already dammed the river partially and  
437 holds potential to completely block the river in near future (Kumar et al. 2019a). Run-out  
438 analysis of these landslides (S.N. 7, 14, 15, 19) has predicted  $25.6 \pm 2.1$ m,  $24.8 \pm 2.7$ m,  $25.0 \pm$   
439  $4.0$ m and  $26.3 \pm 1.8$ m flow height, respectively that will result in temporary blocking of the  
440 river (Fig. 13,14). These findings of run-out indicate ~~towards~~ the blocking of river in the event  
441 of slope failure, irrespective of durability, despite the conservative depth as input because only  
442  $\frac{1}{4}$  of landslide thickness is used in the run-out analysis (sec. 3.5).

443 Stability evaluation of these five landslide slopes (S.N. 5, 7, 14, 15, 19) that have potential to  
444 form landslide dam revealed that ~~except one landslide (S.N.7) that is meta-stable,~~ remaining  
445 ~~four~~ belong to the unstable category (Fig. 4). Further, ~~except this landslide that is meta-stable~~  
446 ~~(S.N. 7), remaining~~ four unstable landslide slopes are debris slide in nature. It is noteworthy to  
447 discuss the implications of  $FS < 1$ . The Factor of Safety (FS) in the Shear Strength Reduction  
448 (SSR) approach is a factor by which the existing shear strength of material is divided to  
449 determine the critical shear strength at which failure occurs (Zienkiewicz et al. 1975; Duncan  
450 1996). Since the landslide represents a failed slope i.e., critical shear strength  $>$  existing shear  
451 strength,  $FS < 1$  is justifiable. Further, the failure state of a slope in the FEM can be defined by  
452 different criteria; the FS of same slope may vary a little depending upon the usage of failure  
453 criteria and the convergence threshold (Abramson et al. 1996; Griffiths and Lane 1999).

454 The possible causes of instability ( $FS < 1$ ) may be steep slope gradient, rockmass having low  
455 strength, and joints. Three (S.N. 7, 14, 15) out of these ~~five~~ landslides that have potential to

456 form the dam belong to the tectonically active Higher Himalaya Crystalline (HHC). The notion  
457 of steep slope gradient cannot be generalized because the HHC accommodates most  
458 voluminous ( $\sim 10^5$ - $10^7$  m<sup>3</sup>) landslides (Fig. 4). These deep seated landslides must require  
459 smooth slope gradient to accommodate the voluminous overburden. Further, the HHC  
460 comprises i.e., gneiss having high compressive strength and Geological Strength Index  
461 (Supplementary Table 2, Kumar et al. 2020), therefore the notion of low strength rockmass  
462 also may not be appropriate. However, the jointed rock mass that owes its origin to numerous  
463 small scale folds, shearing, and faults associated with the active orogeny process can be  
464 considered as the main factor for relatively more instability of debris slide type landslides.  
465 Since, the study area is subjected to the varied stress regime caused by the tectonic structures  
466 (Vannay et al. 2004), thermal variations (Singh et al. 2015), and anthropogenic cause (Lata et  
467 al. 2015), joints may continue to develop and destabilize the slopes. Apart from this inherent  
468 factor like joints, external factors like rainfall and exhumation rate may also contribute to  
469 instability of these landslides. This region receives relatively more annual rainfall owing to  
470 orographic barrier setting (Fig. 11) and is subjected to relatively high exhumation rate of 2.0-  
471 4.5 mm/yr (Thiede et al. 2009).

472 Two landslides (S.N. 5, 19) that are also capable to form potential landslide dam (Fig. 8, 9a; e)  
473 and are also unstable (FS<1) in nature (Fig. 4) do not belong to the HHC. The first landslide  
474 (S.N. 5) exists at the lithological contact of schist of the Tethyan Sequence and Kinnaur Kailash  
475 Granite rockmass. A regional normal fault, i.e., Sangla Detachment (SD), passes through this  
476 contact. Few studies suggest that the SD is an outcome of reactivation of former thrust fault  
477 that has resulted in intense rockmass shearing (Vannay et al. 2004; Kumar et al. 2019b). Owing  
478 to its location in the orographic interior region, hillslopes receives very low annual rainfall  
479 (Fig. 11) and thus comprises least vegetation on the hillslopes. The lack of vegetation on  
480 hillslopes has been observed to result in low shear strength of material and hence in the  
481 instability (Kokutse et al. 2016). Thus, lithological contrast, rockmass shearing, and lack of  
482 vegetation are the main reasons of instability of S.N. 5 landslide. The second landslide (S.N.  
483 19) belongs to the inter-layered schist/gneiss rockmass of the Lesser Himalaya Crystalline  
484 (LHC) and is situated at the orographic front where rainfall increases suddenly (Fig. 11).  
485 Further, this region is also subjected to the high exhumation rate of 2.0-4.5 mm/yr (Thiede et  
486 al. 2009). Therefore, lithological contrast, high rainfall and high exhumation rate are  
487 considered as the main reasons of instability of this landslide slope.

488 The landslides that ~~could not~~ result into the river damming are mostly in the LHC and Lesser  
489 Himalaya Sequence (LHS) region. These regions consist of a majority of the rock fall and rock  
490 avalanches that are generally of meta-stable category (Fig. 4). Despite the narrow valley  
491 setting, landslides in these regions may not form the potential landslide dam, at present, owing  
492 to the relatively ~~less~~ landslide volume. The possible causes of ~~this~~ meta-stability may be high  
493 compressive strength and geological strength index of gneiss (Kumar et al. 2020), dense  
494 vegetation on the hillslopes (Chawla et al. 2012), relatively less sheared rock mass in  
495 comparison to the HHC region, and relatively less decrease in land use/landcover (Lata et al.  
496 2015). Maximum Total Displacement (TD) is also associated with the rock fall and rock  
497 avalanche of this region (Fig. 4).

498 In the parametric study, soil friction and in-situ stress are noted to affect the FS most in case of  
499 the debris slide, whereas the FS of rock fall and rock avalanche are mainly controlled by the  
500 'mi' and the in-situ stress. The 'mi' is a GHB criteria parameter that is equivalent to the friction  
501 in the M-C criteria. For the TD of the debris slides, field stress, elastic modulus and Poisson's  
502 ratio, whereas for rock falls and rock avalanches, 'mi' parameter and in-situ stress played the  
503 dominant role (Fig. 6,7). ~~The~~ friction has been a controlling factor for the shear strength and  
504 its decrease has been observed to result in the shear failure of slope material (Matsui and San  
505 1992). Since ~~the~~ rainfall ~~constitutes~~ an important role in decreasing the friction of slope  
506 material by changing the pore water pressure regime (Rahardjo et al. 2005), frequent extreme  
507 rainfall events in the study area since the year 2013 (Kumar et al. 2019a) amplifies the risk of  
508 hillslope instability. Furthermore, the in-situ field stress that has been compressional and/or  
509 extensional owing to the orogenic setting in the region may also enhance the hillslope  
510 instability (Eberhardt et al. 2004; Vannay et al. 2004). Deformation parameters e.g. elastic  
511 modulus and Poisson's ratio are also observed to affect the displacement in slope models of the  
512 debris slides. Similar studies in other regions have also noted the sensitivity of the elastic  
513 modulus and Poisson's ratio on the slope stability (Zhang and Chen 2006).

514 The study area has been subjected to extreme rainfalls since the year 2010 and received  
515 widespread slope failures and flash-floods (Fig. 11b). Three (S.N. 7,14,15 in Fig. 9) out of five  
516 potential landslide dams belong to the Higher Himalaya Crystalline (HHC) that receives  
517 relatively more rainfall (Fig. 11). Contrary to the along 'Himalayan' arc distribution of  
518 earthquakes, the study area has received most of the earthquakes around the N-S oriented  
519 Kaurik-Chango Fault (Fig. 12a). However, the only major earthquake event has been  $M_w$  6.8  
520 earthquake on 19<sup>th</sup> Jan. 1975 that resulted in the widespread landslides (Khattri et al. 1978).

521 The low-magnitude seismicity in the region has been attributed to the northward extension of  
522 the Delhi-Haridwar ridge (Hazarika et al. 2019), whereas the shallow nature is subjected to the  
523 MHT ramp structure in the region that allows strain accumulation at shallow depth (Bilham  
524 2019). Thus, earthquake has not been a major landslide triggering process in the region. Finally,  
525 the word “active landslide” refers to the hillslope that is still subjected to the slope failures  
526 caused by the various factors. The word “landslide” can be perceived in the following three  
527 ways; pre-failure deformations, failure itself, and post-failure displacement (Terzaghi 1950;  
528 Cruden & Varnes, 1996; Hungr et al., 2014). Landslide slopes in this study pertains to the post-  
529 failure state that are categorized into “unstable” and “meta-stable” stages based on their  
530 existing FS. Furthermore, if an active landslide is not categorized as “unstable”, it means that  
531 the existing slope geometry provides it a “meta-stable” stage that might transform into an  
532 unstable stage with time due to the stability controlling parameters (Sec. 4.1). A supplementary  
533 table involving all the details like landslides dimension, factor of safety, and geomorphic  
534 indices output of each landslide is provided in the data repository (Kumar et al. 2020).

535 In view of the possible uncertainties in the predictive nature of study, following assumptions  
536 ~~and then resolutions~~ were made;

- 537 • To account the effect the spatial variability in the slope geometry, 3D models have been  
538 in use for the last decade (Griffiths and Marquez 2007). However, the pre-requisite for  
539 the 3D models involves the detailed understanding of slope geometry and material  
540 variability in the subsurface that was not possible in the study area considering steep  
541 and inaccessible slopes. Therefore, multiple 2D sections were chosen, wherever  
542 possible. To account the effect of sampling bias and material variability, a range of  
543 values of input parameters was used (sec. 4.1).
- 544 • Determination of the debris thickness has been a major problem in the landslide volume  
545 measurement particularly in the steep, narrow river valleys of the NW Himalaya.  
546 Therefore, the thickness was approximated by considering the relative altitude of the  
547 ground on either side of the deposit, as also performed by Innes (1983). It was assumed  
548 that the ground beneath the deposit is regular.
- 549 • The resultant dam volume could be different from the landslide volume due to the  
550 entrainment, rockmass fragmentation, pore water pressure, size of debris particles, and  
551 washout of landslide material by the river (Hungr and Evans 2004; Dong et al. 2011;  
552 Yu et al. 2014). Therefore, dam volume is presumed to be equal to landslide volume  
553 for the worst-case scenario (sec. 3.3). Stream power is manifested by the upstream

554 catchment area and local slope gradient in the geomorphic indices. It may also vary at  
555 temporal scale owing to the temporally varying water influx from glaciers and  
556 precipitation systems i.e., ISM and WD (Gadgil et al. 2007; Hunt et al. 2018). Though  
557 our study is confined to the spatial scale at present, the findings remain subjected to the  
558 change at temporal scale.

559 • The RAMMS model (Voellmy 1955; Salm 1993; Christen et al. 2010) requires the  
560 calibrated friction and turbulence values for the run-out analysis. Though the previous  
561 debris flow events ~~don't have trace~~ in the study area owing to the convergence of  
562 ~~landslide toe~~ with the river channel, a range of  $\mu$  and  $\xi$  values were used in the study in  
563 view of the material type and run-out path characteristics.

564 Despite these uncertainties, ~~such studies~~ are required to minimize the risk and avert the  
565 possible disasters in the terrain where human population is ~~bound to live~~ in the proximity  
566 of unstable landslides.

## 567 CONCLUSION

568 Out of forty-four landslides that are studied, five landslides are noted to form the potential  
569 landslide dam, if failure occurs. Though the blocking duration is difficult to predict, upstream  
570 and downstream consequences of these damming events ~~can't be overlooked~~ as the region has  
571 witnessed many damming and flash floods in the past. These five landslides comprise a total  
572 landslide volume of  $26.3 \pm 6.7 \text{ M m}^3$ . The slopes of four landslides (debris slides) out of these  
573 five are unstable, whereas the remaining one (rock avalanche) is meta-stable. Field  
574 observations and previous studies have noted the damming events by these landslides (or the  
575 region consisting these landslides) in the past also. Since the area is witnessing enhanced  
576 rainfall and flash floods since year 2010, findings of the run-out analysis that revealed  $24.8 \pm$   
577  $2.7\text{m}$  to  $39.8 \pm 4.0\text{m}$  high material flow from these landslides become more crucial. The  
578 parametric analysis for the slope stability evaluation revealed that the angle of internal friction  
579 of soil or ' $m_i$ ' (equivalent to the angle of internal friction) of the rockmass, and *in-situ* field  
580 stress are the most controlling parameters for the stability of slopes.

## 581 ACKNOWLEDGEMENT

582 VK and IJ acknowledge the constructive discussion on the regional scale study with Prof. H.B.  
583 Havenith, Prof. D.V. Griffiths, and Prof. D.P. Kanungo. VG and RKB acknowledge the

584 financial help through the project MOES/Indo-Nor/PS-2/2015. Authors are thankful to the  
585 RAMMS developer for the license. Authors are also thankful to Prof. Xuanmei Fan (Associate  
586 Editor) and two anonymous reviewers for their insightful comments that improved the final  
587 manuscript.

#### 588 **Conflict of Interest**

589 The authors declare that they have no conflict of interest.

#### 590 **Dataset Availability**

591 The dataset is uploaded in the open access repository (*Mendeley data*) as Kumar et al. (2020).

#### 592 **Author contribution**

593 VK conceived the idea and collected the field data. VK and IJ performed the laboratory  
594 analysis. All authors contributed to the dataset compilation, numerical simulation and  
595 geomorphic interpretations. All authors contributed to the writing of the final draft.

#### 596 **REFERENCES**

- 597 Abramson, L. W., Lee, T. S., Sharma, S. 1996. "Slope stability and stabilization methods".  
598 New York. Wiley.
- 599 Aydin, A. 2008. "ISRM suggested method for determination of the Schmidt hammer rebound  
600 hardness: revised version". In: R. Ulusay (ed) *The ISRM Suggested Methods for Rock  
601 Characterization, Testing and Monitoring: 2007–2014*. Springer, Cham, pp. 25-33.
- 602 Barton, N. and Bandis, S. 1982. "Effects of block size on the shear behavior of jointed rock".  
603 In: *Proc. 23rd US symposium on rock mechanics*. American Rock Mechanics  
604 Association, 739-760.
- 605 Barton, N. and Choubey, V. 1977. "The shear strength of rock joints in theory and practice".  
606 *Rock mechanics* 10(1-2):1-54.
- 607 Barton, N. R. 1972. "A model study of rock-joint deformation. International journal of rock  
608 mechanics and mining sciences". *Geomech. Abstr.* 9 (5): 579-602.
- 609 Barton, N. R. and Bandis, S. C. 1990. "Review of predictive capabilities pf JRC-JCS model in  
610 engineering practice". In: *Barton N and Stephansson O (ed) Rock Joints*, Rotterdam, pp.  
611 603-610.
- 612 Bhasin, R. and Kaynia, A. M. 2004. "Static and dynamic simulation of a 700-m high rock slope  
613 in western Norway". *Engineering Geology* 71(3-4): 213-226.
- 614 Bilham, R. 2019. "Himalayan earthquakes: a review of historical seismicity and early 21st  
615 century slip potential". *Geological Society, London, Special Publications*. 483(1):423-  
616 82.
- 617 Bowles, J. E. 1996. *Foundation Analysis and Design, 5<sup>th</sup> ed.*, McGraw-Hill, New York, pp. 750.

618 Braun, A., Cuomo, S., Petrosino, S., Wang, X. and Zhang, L., 2018. "Numerical SPH analysis  
619 of debris flow run-out and related river damming scenarios for a local case study in SW  
620 China". *Landslides* 15 (3), 535-550.

621 Cai, M., Kaiser, P. K., Tasaka, Y. and Minami, M. 2007. "Determination of residual strength  
622 parameters of jointed rock masses using the GSI system". *International Journal of Rock  
623 Mechanics and Mining Sciences* 44(2): 247-265.

624 Chawla, A., Kumar, A., Lal, B., Singh, R.D. and Thukral, A.K. 2012. "Ecological  
625 Characterization of High Altitude Himalayan Landscapes in the Upper Satluj River  
626 Watershed, Kinnaur, Himachal Pradesh, India". *Journal of the Indian Society of Remote  
627 Sensing* 40(3): 519-539.

628 Cho, S. E. 2007. "Effects of spatial variability of soil properties on slope stability". *Engineering  
629 Geology* 92(3-4): 97-109.

630 Christen, M., Kowalski, J., Bartelt, P. 2010. "RAMMS: Numerical simulation of dense snow  
631 avalanches in three-dimensional terrain". *Cold Regions Science and Technology*.63: 1-  
632 14.

633 Corominas, J. and Mavrouli, J., 2011. "Living with landslide risk in Europe: Assessment,  
634 effects of global change, and risk management strategies". *Documento tecnico, safeland.  
635 7<sup>th</sup> Framework Programme Cooperation Theme, 6.*

636 Costa, J. E. and Schuster, R. L. 1988. "The formation and failure of natural dams". *Geological  
637 society of America bulletin* 100(7): 1054-1068.

638 Coulomb, C. A. 1776. "An attempt to apply the rules of maxima and minima to several  
639 problems of stability related to architecture". *Mémoires de l'Académie Royale des  
640 Sciences* 7: 343-382.

641 Cruden, D. M. and Varnes, D. J. 1996. Landslides: investigation and mitigation. In: Landslide  
642 types and processes. Transportation Research Board, US National Academy of Sciences,  
643 Special Report, (247).

644 Dai, F.C., Lee, C.F., Deng, J.H. and Tham, L.G. 2005. "The 1786 earthquake-triggered  
645 landslide dam and subsequent dam-break flood on the Dadu River, southwestern China".  
646 *Geomorphology* 65(3): 205-221.

647 Deere, D. U. and Miller, R. P. 1966. "Engineering classification and index properties for intact  
648 rock". Illinois University at Urbana, USA.

649 Delaney, K. B. and Evans, S. G. 2015. "The 2000 Yigong landslide (Tibetan Plateau), rockslide-  
650 dammed lake and outburst flood: review, remote sensing analysis, and process  
651 modelling". *Geomorphology* 246, 377-393.

652 Dimri, A.P., Niyogi, D., Barros, A.P., Ridley, J., Mohanty, U.C., Yasunari, T. and Sikka, D.R.  
653 2015. "Western disturbances: A review". *Reviews of Geophysics* 53(2): 225-246

654 Dong, J.J., Tung, Y.H., Chen, C.C., Liao, J.J. and Pan, Y.W. 2011. "Logistic regression model  
655 for predicting the failure probability of a landslide dam". *Engineering Geology* 117(1):  
656 52-61.

657 Duncan, J. M. 1996. "State of art: limit equilibrium and finite element analysis of slopes".  
658 *Journal of Geotechnical Engineering Division, ASCE* 122 (7): 577-596.

659 Eberhardt, E., Stead, D. and Coggan, J. S. 2004. "Numerical analysis of initiation and  
660 progressive failure in natural rock slopes—the 1991 Randa rockslide". *International  
661 Journal of Rock Mechanics and Mining Sciences* 41(1): 69-87.

662 Ermini, L. and Casagli, N. 2003. "Prediction of the behaviour of landslide dams using a  
663 geomorphological dimensionless index". *Earth Surface Processes and Landforms* 28(1):  
664 31-47.

665 Fan, X, Dufresne, A, Subramanian, SS, Strom, A, Hermanns, R, Stefanelli, CT, Hewitt, K,  
666 Yunus, AP, Dunning, S, Capra, L and Geertsema, M. 2020. "The formation and impact  
667 of landslide dams—State of the art". *Earth-Science Reviews*, 203:103116.

668 Fujisawa, K., Kobayashi, A. and Aoyama, S. 2009. "Theoretical description of embankment  
669 erosion owing to overflow". *Geotechnique* 59(8): 661-671.

670 Gadgil, S., Rajeevan, M. and Francis, P.A. 2007. "Monsoon variability: Links to major  
671 oscillations over the equatorial Pacific and Indian oceans". *Current Science*. 93(2):182-  
672 94.

673 Griffiths, D. V. and Lane, P. A. 1999. "Slope stability analysis by finite elements".  
674 *Geotechnique* 49(3): 387-403.

675 Griffiths, D. V. and Marquez, R. M. 2007. "Three-dimensional slope stability analysis by  
676 elasto-plastic finite elements". *Geotechnique* 57(6): 537-546.

677 Gupta, V. and Sah, M. P. 2008. "Impact of the trans-Himalayan landslide lake outburst flood  
678 (LLOF) in the Satluj catchment, Himachal Pradesh, India". *Natural Hazards* 45(3): 379-  
679 390.

680 Gupta, V. Nautiyal, H., Kumar, V., Jamir, I., and Tandon, R. S. 2016. "Landslides hazards  
681 around Uttarkashi Township, Garhwal Himalaya, after the tragic flash flood in June  
682 2013". *Natural Hazards* 80: 1689-1707

683 Hungr, O., Leroueil, S., and Picarelli, L. 2014. "The Varnes classification of landslide types,  
684 an update". *Landslides* 11 (2): 167-194.

685 Hürlimann, M., Rickenmann, D., Medina, V. and Bateman, A. 2008. "Evaluation of approaches  
686 to calculate debris-flow parameters for hazard assessment". *Eng Geol* 102:152–163

687 Havenith, H.B., Torgoev, I. and Ischuk, A. 2018. "Integrated Geophysical-Geological 3D  
688 Model of the Right-Bank Slope Downstream from the Rogun Dam Construction Site,  
689 Tajikistan". *International Journal of Geophysics* 1-17.

690 Hazarika, D., Wadhawan, M., Paul, A., Kumar, N. and Borah, K. 2017. "Geometry of the Main  
691 Himalayan Thrust and Moho beneath Satluj valley, northwest Himalaya: Constraints  
692 from receiver function analysis". *Journal of Geophysical Research: Solid Earth*.  
693 122(4):2929-45.

694 Hoek, E. and Brown, E.T. 1997. "Practical estimates of rock mass strength". *International*  
695 *Journal of Rock Mechanics and Mining Science* 34(8):1165-1186

696 Hoek, E. and Diederichs, M.S. 2006. "Empirical estimation of rock mass modulus".  
697 *International Journal of Rock Mechanics and Mining Sciences* 43 (2): 203-15.

698 Hoek, E., Kaiser, P.K. and Bawden, W.F. 1995. *Support of Underground Excavations in Hard*  
699 *Rock*. Rotterdam: A. A. Balkema.

700 Hungr, O. and Evans, S.G. 2004. "Entrainment of debris in rock avalanches: an analysis of a  
701 long run-out mechanism". *Geological Society of America Bulletin* 116(9-10): 1240-1252.

702 Hungr, O., Morgan, G.C. and Kellerhals, R. 1984. "Quantitative analysis of debris torrent  
703 hazards for design of remedial measures". *Can Geotech J* 21:663–677

704 Hunt, K.M., Turner, A.G. and Shaffrey, L.C. 2018. “The evolution, seasonality and impacts of  
705 western disturbances”. *Quarterly Journal of the Royal Meteorological Society*.  
706 144(710):278-90.

707 Hutter, K., Svendsen, B. and Rickenmann, D. 1994. “Debris flow modelling: a review”.  
708 *Continuum mechanics and thermodynamics* 8: 1-35.

709 Innes, J. L. 1983. “Debris flows”. *Progress in Physical Geography* 7(4): 469–501.

710 IS: 2720 (Part 10)–1991. “Method of test for soils: Determination of unconfined compressive  
711 strength”. *In: Bureau of Indian Standards, Delhi, India*.

712 IS: 2720 (Part 13)–1986. “Method of test for soils: Direct shear test”. *In: Bureau of Indian  
713 Standards, New Delhi, India*.

714 IS: 2720 (Part 4)–1985. “Methods of test for soils: Grain size analysis”. *In: Bureau of Indian  
715 Standards, New Delhi, India*.

716 IS: 9143-1979. “Method for the determination of unconfined compressive strength of rock  
717 materials”. *In: Bureau of Indian Standards, New Delhi, India*.

718 Jamir, I., Gupta, V., Kumar, V. and Thong, G.T. 2017. “Evaluation of potential surface  
719 instability using finite element method in Kharsali Village, Yamuna Valley, Northwest  
720 Himalaya”. *Journal of Mountain Science* 14(8): 1666-1676.

721 Jamir, I., Gupta, V., Thong, G.T. and Kumar, V. 2019. “Litho-tectonic and precipitation  
722 implications on landslides, Yamuna valley, NW Himalaya”. *Physical Geography* 41(4)  
723 365-388.

724 Jang, H.S., Kang, S.S. and Jang, B.A. 2014. “Determination of joint roughness coefficients  
725 using roughness parameters”. *Rock mechanics and rock engineering* 47(6): 2061-73.

726 Jing, L. 2003. “A review of techniques, advance and outstanding issues in numerical modelling  
727 for rock mechanics and rock engineering”. *International Journal of Rock Mechanics and  
728 Mineral Science* 40:283-353.

729 Khattri, K., Rai, K., Jain, A.K., Sinvhal, H., Gaur, V.K. and Mithal, R.S. 1978. “The Kinnaur  
730 earthquake, Himachal Pradesh, India, of 19 January, 1975”. *Tectonophysics*. 49(1-2):1-  
731 21.

732 Kokutse, N.K., Temgoua, A.G.T. and Kavazović, Z. 2016. “Slope stability and vegetation:  
733 Conceptual and numerical investigation of mechanical effects”. *Ecological Engineering*  
734 86: 146–153.

735 Kumar, V., Gupta, V. and Jamir, I. 2018. “Hazard Evaluation of Progressive Pawari Landslide  
736 Zone, Kinnaur, Satluj Valley, Higher Himalaya, India”. *Natural Hazards* 93: 1029-1047.

737 Kumar, V., Gupta, V., Jamir, I. and Chattoraj, S.L. 2019a. “Evaluation of potential landslide  
738 damming: Case study of Urni landslide, Kinnaur, Satluj valley, India”. *Geosci. Front.*  
739 10(2): 753-767.

740 Kumar, V., Gupta, V. and Sundriyal, Y.P. 2019b. “Spatial interrelationship of landslides, litho-  
741 tectonics, and climate regime, Satluj valley, Northwest Himalaya”. *Geol. J.* 54: 537–551.

742 Kumar, V., Jamir, I., Gupta, V. and Bhasin, R.K. 2020. “Dataset used to infer regional slope  
743 stability, NW Himalaya”. *Mendeley Data*. DOI: 10.17632/jh8b2rh8nz.1

744 Kundu, B., Yadav, R.K., Bali, B.S., Chowdhury, S. and Gahalaut, V.K. 2014. “Oblique  
745 convergence and slip partitioning in the NW Himalaya: Implications from GPS  
746 measurements.” *Tectonics* 33: 2013-2024.

- 747 Lata, R., Rishi, S., Talwar, D. and Dolma, K. 2015. "Comparative Study of Landuse Pattern in  
748 the Hilly Area of Kinnaur District, Himachal Pradesh, India". *International Journal of*  
749 *Innovative Science, Engineering & Technology* 2(4): 559-565.
- 750 Li, D.Q., Qi, X.H., Cao, Z.J., Tang, X.S., Phoon, K.K. and Zhou, C.B. 2016. "Evaluating slope  
751 stability uncertainty using coupled Markov chain". *Computers and Geotechnics* 73:72-82.
- 752 Li, T., Schuster, R.L. and Wu, J. 1986. "Landslide dams in south-central China". In: *Proc.*  
753 *Landslide dams: processes, risk, and mitigation*, ASCE Convention, Washington, 146-  
754 162.
- 755 Li, M.H., Sung, R.T., Dong, J.J., Lee, C.T., and Chen, C.C. 2011. "The formation and breaching  
756 of a short-lived landslide dam at Hsiaolin village, Taiwan-Part II: Simulation of debris  
757 flow with landslide dam breach". *Engineering Geology* 123: 60-71.
- 758 Martha, T.R., Kerle, N., Jetten, V., van Westen, C.J. and Kumar, K.V. 2010. "Landslide  
759 volumetric analysis using Cartosat-1-derived DEMs". *IEEE Geoscience and remote*  
760 *sensing letters* 7(3): 582-586.
- 761 Matsui, T. and San, K.C. 1992. "Finite element slope stability analysis by shear strength  
762 reduction technique". *Soils and foundations* 32(1): 59-70.
- 763 Mohr, O. 1914. "Abhandlungen aus dem Gebiete der Technischen Mechanik" (2nd ed). Ernst,  
764 Berlin.
- 765 NDMA: National Disaster Management Authority. 2013. Annual report, Government of India,  
766 Delhi.
- 767 Nian, T.K., Chen, G.Q., Wan, S.S. and Luan, M.T. 2011. "Non-convergence Criterion on Slope  
768 Stability FE Analysis by Strength Reduction Method". *Journal of Convergence*  
769 *Information Technology* 6:78-88.
- 770 O'Brien, J.S., Julien, P.Y. and Fullerton, W.T. 1993. "Two-dimensional water flood and mud  
771 flood simulation". *J Hydraul Eng* 119:244-260.
- 772 Parkash, S. 2011. "Historical records of socio-economically significant landslides in India". *J*  
773 *South Asia Disaster Studies* 4(2): 177-204.
- 774 Rahardjo, H., Lee, T.T., Leong, E.C. and Rezaur, R.B. 2005. "Response of a residual soil slope  
775 to rainfall". *Canadian Geotechnical Journal* 42(2): 340-351.
- 776 Rickenmann, D. 2005. "Runout prediction methods". In: *Jakob M, Hungr O (eds) Debris-flow*  
777 *hazards and related phenomena*. Praxis/Springer, Berlin/Heidelberg, pp. 305-324.
- 778 Rickenmann, D., and Scheidl, C. 2013. "Debris-Flow Runout and Deposition on the Fan". *M.*  
779 *Schneuwly-Bollschweiler et al. (eds.), Dating Torrential Processes on Fans and Cones,*  
780 *Advances in Global Change Research* 47, DOI 10.1007/978-94-007-4336-6 5
- 781 Ruiz-Villanueva, V., Allen, S., Arora, M., Goel, N. K. and Stoffel, M. 2016. "Recent  
782 catastrophic landslide lake outburst floods in the Himalayan mountain range". *Progress*  
783 *in Physical Geography* 41 (1): 3-28.
- 784 Salm, B., 1993. "Flow, flow transition and runout distances of flowing avalanches". *Ann.*  
785 *Glaciol.* 18: 221-226.
- 786 Sharma, S., Shukla, A.D., Bartarya, S.K., Marh, B.S. and Juyal, N. 2017. "The Holocene floods  
787 and their affinity to climatic variability in the western Himalaya, India". *Geomorphology*  
788 290: 317-334.
- 789 Sharma, K. K. 1977. "A contribution to the geology of Satluj Valley, Kinnaur, Himachal  
790 Pradesh, India". *Collques Internationaux du CNRS* 268: 369-378.

791 Singh, D., Gupta, R.D. and Jain, S.K. 2015.“Statistical analysis of long term spatial and  
792 temporal trends of temperature parameters over Sutlej river basin, India”. *J. Earth Syst.*  
793 *Sci.* 124 (1): 17-35.

794 Stefanelli, C.T., Segoni, S., Casagli, N. and Catani, F. 2016.“Geomorphic indexing of landslide  
795 dams evolution”. *Engineering Geology* 208: 1-10.

796 Takahashi, T. And Nakagawa, H. 1993.“Flood and debris flow hydrograph due to collapse of  
797 a natural dam by overtopping”. *In: Proc. Hydraulic Engineering, Japan*, 37: 699-704.

798 Terzaghi, K. 1950. “Mechanism of Landslides”. *In: Application of Geology to Engineering*  
799 *Practice. Geol. Soc. Am* 83-123.

800 Thiede, R.C., Ehlers, T.A., Bookhagen, B. and Strecker, M.R. 2009.“Erosional variability  
801 along the northwest Himalaya”. *Journal of Geophysical Research: Earth Surface* 114  
802 F101015.

803 Vannay, J.C., Grasemann, B., Rahn, M., Frank, W., Carter, A., Baudraz, V. and Cosca, M.  
804 2004.“Miocene to Holocene exhumation of metamorphic crustal wedges in the NW  
805 Himalaya: Evidence for tectonic extrusion coupled to fluvial erosion”. *Tectonics* 23  
806 TC1014.

807 Voellmy, A. 1955. “On the destructive force of avalanches”, *Translation No. 2. Avalanche*  
808 *Study Center, United States Department of Agriculture, USA.*

809 Wong, F.S. 1984.“Uncertainties in FE modelling of slope stability”. *Computers & structures*  
810 19(5-6): 777-791.

811 Wulf, H., Bookhagen, B. and Scherler, D. 2012.“Climatic and geologic controls on suspended  
812 sediment flux in the Sutlej River Valley, western Himalaya”. *Hydrology and Earth*  
813 *System Sciences* 16(7): 2193-2217.

814 Yu, G., Zhang, M., Chen, H., 2014. “The dynamic process and sensitivity analysis for debris  
815 flow”. *In: Sassa, K., Canuti, P., Yin, Y. (Eds.), Landslide Science for a Safer*  
816 *Geoenvironment.* Springer.

817 Zhang, P. W. and Chen, Z. Y. 2006.“Influences of soil elastic modulus and Poisson's ratio on  
818 slope stability”. *YantuLixue (Rock and Soil Mechanics)* 27(2): 299-303.

819 Zienkiewicz, O. C., Humpheson, C. and Lewis, R. W. 1975.“Associated and non-associated  
820 viscoplasticity and plasticity in soil mechanics”. *Geotechnique* 25(4): 671-689.

821 **LIST OF FIGURES AND TABLES**

822 **Fig. 1** Geological setting. WGC: Wangtu Gneissic Complex. The red dashed circle in the inset  
823 represents the region within 100 km radius from the Satluj River (marked as blue line) that  
824 was used to determine the earthquake distribution in the area. KCF in inset refers to  
825 Kaurik-Chango Fault. The numbers 1-44 refer to serial number of landslides in Table 1.

826 **Fig. 2** Field photographs of some of the landslides (a) Khokpa landslide (**S.N.1**); (b) Akpa\_III  
827 landslide (**S.N. 5**); (c) Rarang landslide (**S.N. 6**); (d) Pawari landslide (**S.N.14**); (e) Urni  
828 landslide (**S.N.19**); (f) Barauni Gad\_I\_S landslide (**S.N. 38**). Black circle in the pictures  
829 that encircles the vehicle is intended to represent the relative scale.

830 **Fig. 3** The FEM configuration of some of the slope models. S.N. refers to the serial no. of  
831 landslides in Table 1. The joint distribution in all the slopes was parallel-statistical with  
832 the normal distribution of joint spacing.

833 **Fig. 4** The FEM analysis of all forty-four landslides. Grey bar in the background highlights  
834 the Higher Himalaya Crystalline (HHC) region that comprises relatively more unstable  
835 landslides, relatively more landslide volume and human population. Source of human  
836 population: Census 2011 (Govt. of India, New Delhi). TS, KKG, HHC, LHC and LHS are  
837 Tethyan Sequence, Kinnaur Kailash Granite, Higher Himalaya Crystalline, Lesser  
838 Himalaya Crystalline and Lesser Himalaya Sequence, respectively

839 **Fig. 5** Relationship of Factor of Safety (FS), Total Displacement (TD) and Shear Strain (SS).  
840 DS, RF, and RA refer to Debris slide, rock fall and rock avalanche, respectively.

841 **Fig. 6** Parametric analysis of debris slides. (a) Akpa\_III (S.N. 5); (b) Pangi\_III (S.N. 13); (c)  
842 Barauni Gad\_I\_S (S.N. 38). S. N. refers to the serial no. of landslides in Table 1.

843 **Fig. 7** Parametric analysis of rockfall/rock avalanche. (a) Tirung khad (S.N. 2); (b) Baren  
844 Dogri (S.No. 7); (c) Chagaon\_II (S.N. 21).

845 **Fig. 8** Landslide damming indices (a) Morphological Obstruction Index (MOI); (b) Hydro-  
846 morphological dam stability index (HDSI); (c) Landslides vs. MOI; (d) Landslides vs.  
847 HDSI.

848 **Fig. 9** Potential landslide damming locations. (a) Akpa\_III landslide; (b) Baren dogri  
849 landslide; (c) Pawari landslide; (d) Telangi landslide; (e) Urni landslide.

850 **Fig. 10** Field signatures of the landslide damming near Akpa\_III landslide. (a) Upstream view  
851 of Akpa landslide with lacustrine deposit at the left bank; (b) enlarged view of the  
852 lacustrine deposit with an arrow indicating the lacustrine sequence; (c) alternating fine-  
853 coarse sediments. F and C refer to fine (covered by yellow dashed lines) and coarse  
854 (covered by green dashed lines) sediments, respectively.

855 **Fig. 11** Rainfall distribution. (a) Topographic profile; (b) annual rainfall; (c) monsoonal (June-  
856 Sep.) rainfall; (d) non-monsoonal (Oct.-May) rainfall. Green bars represent the years of  
857 relatively more rainfall resulting into the flash floods, landslides and socio-economic loss  
858 in the region. (i):[hpenvis.nic.in](http://hpenvis.nic.in), retrieved on March 1, 2020; Department of Revenue,

859 Govt. of H.P. (ii): hpenvis.nic.in, retrieved on March 1, 2020.(iii): Kumar et al.,  
860 2019a;ndma.gov.in, retrieved on march 1, 2020 (iv):sandrp.in, retrieved on march 1,  
861 2020.The numbers 1-44 refer to serial number of the landslides.

862 **Fig. 12** Earthquake distribution. (a) Spatial variation of earthquakes. The transparent circle  
863 represents the region within 100 km radius from the Satluj River (blue line). The black  
864 dashed line represents the seismic dominance around the Kaurik-Chango fault;(b)  
865 earthquake magnitude vs. focal depth. The red dashed region highlights the concentration  
866 of earthquakes within 40 km depth; (c) Cross section view (Based on Hazarika et al. 2017;  
867 Bilham 2019). Red dashed circle represents the zone of strain accumulation caused by the  
868 Indian and Eurasian plate collision (Bilham 2019). ISC: International Seismological  
869 Centre. HFT: Himalayan Frontal Thrust.

870 **Fig. 13** Results of the run-out analysis.  $\mu$  refers to coefficient of friction.

871 **Fig. 14** Results of run-out analysis at different values of  $\mu$  and  $\xi$ .  $\mu$  and  $\xi$  refer to coefficient of  
872 friction and turbulence, respectively.

873 **Table 1** Details of the landslides used in the study.

874 **Table 2** Details of the satellite imagery.

875 **Table 3** Criteria used in the Finite Element Method (FEM) analysis.

876 **Table 4** Details of input parameters used in the run-out analysis.

S.N.	Landslide location	Latitude/ Longitude	Type	Area <sup>1</sup> , m <sup>2</sup>	Volume <sup>2</sup> , m <sup>3</sup>	Human population <sup>3</sup>	Litho- tectonic division
1	Khokpa	31°35'18.9"N 78°26'28.6"E	Debris slide	21897± 241	43794± 18361	373	Tethyan Sequence (TS)
2	Tirung Khad	31°34'50.4"N 78°26'20.5"E	Rockfall	28537± 314	14269± 9055	0	
3	Akpa_I	31°34'57.1"N 78°24'30.6"E	Rock avalanche	963051± 10594	1926102± 807515	0	TS-KKG
4	Akpa_II	31°35'2.2"N 78°23'25.4"E	Rock avalanche	95902± 1055	143853± 40734	470	Kinnaur Kailash Granite (KKG)
5	Akpa_III	31°34'54.5"N 78°23'2.4"E	Debris slide	379570± 4175	7591400± 3182681	1617	
6	Rarang	31°35'58.7"N 78°20'39.1"E	Rockfall	4586± 50	4586± 1923	848	Higher Himalaya Crystalline (HHC)
7	Baren Dogri	31°36'23.6"N 78°20'23.1"E	Rock avalanche	483721± 5321	2418605±421561	142	
8	Thopan Dogri	31°36'12.3"N 78°19'50.4"E	Rockfall	55296± 608	165888± 46974	103	
9	Kashang Khad_I	31°36'5.0"N 78°18'44.4"E	Debris slide	113054± 1244	169581± 48019	103	
10	Kashang Khad_II	31°35'58.3"N 78°18'34.0"E	Rockfall	27171± 299	40757± 11541	103	
11	Pangi_I	31°35'36.4"N 78°17'36.4"E	Debris slide	30112± 331	45168± 12790	1389	
12	Pangi_II	31°35'38.9"N 78°17'12.2"E	Debris slide	59436± 654	118872± 49837	1389	
13	Pangi_III	31°34'38.9"N 78°16'55.6"E	Debris slide	75396± 829	188490± 32854	7	
14	Pawari	31°33'49.8"N 78°16'28.6"E	Debris slide	320564± 3526	1602820± 279370	4427	
15	Telangi	31°33'7.0"N 78°16'37.2"E	Debris slide	543343± 5977	13583575± 2367608	6817	
16	Shongthong	31°31'13.0"N 78°16'17.0"E	Debris slide	5727± 63	11454± 2464	388	
17	Karchham	31°30'12.4"N 78°11'30.8"E	Rock avalanche	28046± 309	56092± 23516	0	
18	Choling	31°31'17.0"N 78° 8'4.9"E	Debris slide	20977± 231	20977± 8795	0	Lesser Himalaya Crystalline (LHC)
19	Urni	31°31'8.0"N 78° 7'42.2"E	Debris slide	112097± 1233	1120970± 469965	500	
20	Chagaon_I	31°30'55.9"N 78° 6'52.0"E	Rockfall	3220± 35	3220± 1350	0	
21	Chagaon_II	31°30'57.9"N 78° 6'47.7"E	Rockfall	11652± 128	11652± 4885	0	

22	Chagaon_III	31°31'3.0"N 78° 6'21.4"E	Debris slide	42141± 464	168564± 70670	1085	
23	Wangtu_U/s	31°32'4.8"N 78° 3'5.0"E	Rock avalanche	211599± 2328	317399± 89876	17	
24	Wangtu D/s_1	31°33'27.7"N 77°59'43.7"E	Debris slide	4655± 51	9310± 3903	71	
25	Kandar	31°33'43.7"N 77°59'54.9"E	Rock avalanche	151128± 1662	302256± 126720	186	
26	Wangtu D/s_2	31°33'38.9"N 77°59'29.9"E	Debris slide	8004± 88	16008± 6711	71	
27	Agade	31°33'52.3"N 77°58'3.5"E	Debris slide	9767± 107	14651± 4149	356	
28	Punaspa	31°33'37.6"N 77°57'31.5"E	Debris slide	3211± 35	3211± 1346	343	
29	Sungra	31°33'58.8"N 77°56'49.6"E	Debris slide	5560± 61	11120± 4662	2669	
30	Chota Kamba	31°33'39.2"N 77°54'39.0"E	Rock avalanche	197290± 2170	591870± 167597	401	
31	Bara Kamba	31°34'10.4"N 77°52'56.7"E	Rockfall	36347± 400	18174± 7619	564	
32	Karape	31°33'44.9"N 77°53'13.9"E	Debris slide	50979± 561	50979± 21373	1118	
33	Pashpa	31°34'40.2"N 77°50'53.0"E	Rockfall	16079± 171	8040± 3371	29	
34	Khani Dhar_I	31°33'43.4"N 77°48'52.5"E	Rock avalanche	218688± 2406	874752± 366738	0	
35	Khani Dhar_II	31°33'26.3"N 77°48'35.8"E	Rock avalanche	146994± 1617	734970± 248125	0	
36	Khani Dhar_III	31°33'20.1"N 77°48'27.8"E	Rock avalanche	20902± 230	62706± 17756	0	
37	Jeori	31°31'58.8"N 77°46'18.2"E	Rock avalanche	93705± 1031	93705± 39286	0	
38	Barauni Gad_I_S	31°28'56.6"N 77°41'40.4"E	Debris slide	63241± 696	758892± 111620	236	LHC-LHS
39	Barauni Gad_I_Q	31°29'00.0"N 77°41'38.0"E	Debris slide	59273± 652	711276± 104616	0	
40	Barauni Gad_II	31°28'43.9"N 77°41'24.6"E	Rockfall	6977± 77	3489± 1463	0	
41	Barauni Gad_III	31°29'5.6"N 77°41'23.7"E	Rockfall	33115± 364	33115± 13883	0	
42	D/s Barauni Gad_I	31°28'24.9"N 77°41'8.4"E	Rockfall	19101± 210	19101± 8008	0	
43	D/s Barauni Gad_II	31°28'25.5"N 77°40'56.7"E	Rockfall	21236± 234	21236± 8903	0	
44	D/s Barauni Gad_III	31°28'7.4"N 77°40'42.4"E	Rockfall	15632± 172	15632± 6554	0	Lesser Himalaya Sequence (LHS)

<sup>1</sup>Error ( $\pm$ ) caused by GE measurement (1.06 %).

<sup>2</sup>Error ( $\pm$ ) is an outcome of multiplication of area  $\pm$  error and thickness  $\pm$  error. Thickness error (Std. dev.) corresponds to averaging of field based approximated thickness.

<sup>3</sup>The human population is based on census 2011, Govt. of India. The villages/town in the radius of 500 m from the landslide are considered to count the human population.

**Table 1** Details of landslides used in the study.

Satellite data		Source	Date of data	Spatial resolution
CARTOSAT-1 stereo imagery	524/253	National Remote Sensing Center (NRSC), Hyderabad, India	5 <sup>th</sup> Dec. 2010	~2.5 m
	525/253		16 <sup>th</sup> Dec. 2010	~2.5 m
	526/252		18 <sup>th</sup> Oct. 2011	~2.5 m
	526/253		18 <sup>th</sup> Oct. 2011	~2.5 m
	527/252		24 <sup>th</sup> Nov. 2010	~2.5 m
	527/253		27 <sup>th</sup> Dec. 2010	~2.5 m
	528/252		26 <sup>th</sup> Nov. 2011	~2.5 m

**Table 2** Details of the satellite imagery.

**Table 3** Criteria used in the Finite Element Method (FEM) analysis.

	Material Criteria	Parameters	Source
Rockmass	<p><b>Generalized Hoek &amp; Brown (GHB) Criteria</b> (Hoek et al. 1995)</p> $\sigma_1 = \sigma_3 + \sigma_{ci} [m_b (\sigma_3 / \sigma_{ci}) + s]^a$ <p>Here, <math>\sigma_1</math> and <math>\sigma_3</math> are major and minor effective principal stresses at failure; <math>\sigma_{ci}</math>, compressive strength of intact rock; <math>m_b</math>, a reduced value of the material constant (<math>m_i</math>) and is given by;</p> $m_b = m_i e^{[(GSI-100)/(28-14D]}$ <p>s and a; constants for the rock mass given by the following relationships;</p> $s = e^{[(GSI-100)/(9-3D]}$ $a = \frac{1}{2} + \frac{1}{6} \left[ e^{[-\frac{GSI}{15}]} - e^{[-\frac{20}{3}]} \right]$ <p>Here, D; a factor which depends upon the degree of disturbance to which the rock mass has been subjected by blast damage and stress relaxation. GSI (Geological Strength Index); a rockmass characterization parameter.</p>	Unit Weight, $\gamma$ (MN/m <sup>3</sup> )	Laboratory analysis (UCS) (IS: 9143-1979)
		Uniaxial Compressive Strength, $\sigma_{ci}$ (MPa)	
		Rockmass modulus (MPa)	Laboratory analysis (Ultrasonic velocity test); Hoek and Diederichs (2006).
		Poisson's Ratio	
		Geological Strength Index	Field observation and based on recent amendments (Cai et al. 2007 and reference therein)
		Material Constant ( $m_i$ )	Standard values (Hoek and Brown 1997)
		$m_b$	GSI was field dependent, $m_i$ as per (Hoek and Brown 1997) and D is used between 0-1 in view of rockmass exposure and blasting.
		s	
		a	
		D	
Joint	<p><b>Barton-Bandis Criteria</b> (Barton and Choubey 1977; Barton and Bandis 1990)</p> $\tau = \sigma_n \tan [\phi_r + JRC \log_{10} (JCS / \sigma_n)]$ <p>Here, <math>\tau</math> is joint shear strength; <math>\sigma_n</math>, normal stress across joint; <math>\phi_r</math>, reduced friction angle; JRC, joint roughness coefficient; JCS, joint compressive strength.</p> <p>JRC is based on the chart of Barton and Choubey (1977); Jang et al. (2014). JCS was determined using following equation;</p> $\log_{10}(JCS) = 0.00088 (R_L)(\gamma) + 1.01$ <p>Here, <math>R_L</math> is Schmidt Hammer Rebound value and <math>\gamma</math> is unit weight of rock.</p> <p>The JRC and JCS were used as <math>JRC_n</math> and <math>JCS_n</math>, following the scale corrections observed by Barton and Choubey</p>	Normal Stiffness, $k_n$ (MPa/m)	$E_i$ is lab dependent. L and GSI were field dependent. D is used between 0-1 in view of rockmass exposure and blasting.
		Shear Stiffness, $k_s$ (MPa/m)	It is assumed as $k_n/10$ . However, effect of denominator is also obtained through parameteric study.
		Reduced friction angle, $\phi_r$	Standard values (Barton and Choubey 1977).
		Joint roughness coefficient, JRC	Field based data from profilometer and standard values from Barton and Choubey (1977); Jang et al. (2014).

Soil	<p>(1977) and reference therein and proposed by Barton and Bandis (1982).</p> $JRC_n = [JRC(L/L_o)^{-0.02(JRC)}]$ $JCS_n = [JCS(L/L_o)^{-0.03(JRC)}]$ <p>Here, <math>L</math> and <math>L_o</math> are mean joint spacing in field and, respectively. <math>L_o</math> has been suggested to be 10 cm.</p> <p style="text-align: center;"><b>Joint stiffness criteria</b> (Barton 1972)</p> $k_n = (E_i * E_m) / L * (E_i - E_m)$ <p>Here, <math>k_n</math>; Normal stiffness, <math>E_i</math>; Intact rock modulus, <math>E_m</math>; Rockmass modulus <math>L</math>; Mean joint spacing.</p> $E_m = (E_i) * [0.02 + \{1 - D/2\} / \{1 + e^{(60 + 15 * D - GSD)/11}\}]$ <p>Here, <math>E_m</math> is based on Hoek and Diederichs (2006) and reference therein</p>	Joint compressive strength, JCS (MPa)	Empirical equation of Deere and Miller (1966) relating Schmidt Hammer Rebound (SHR) values, $\sigma_{ci}$ and unit weight of rock. SHR was field dependent.
		Scale corrected, $JRC_n$	Empirical equation of Barton and Bandis (1982).
		Scale corrected, $JCS_n$ (MPa)	
		<p style="text-align: center;"><b>Mohr-Coulomb Criteria</b> (Coulomb 1776; Mohr 1914)</p> $\tau = C + \sigma \tan \phi$ <p>Here, <math>\tau</math>; Shear stress at failure, <math>C</math>; Cohesion, <math>\sigma_n</math>; normal strength, <math>\phi</math>; angle of friction.</p>	Unit Weight (MN/m <sup>3</sup> )
Young's Modulus, $E_i$ (MPa)	Laboratory analysis (UCS); IS: 2720-Part 10-1991.		
Poisson's Ratio	Standard values from Bowles (1996)		
Cohesion, $C$ (MPa)	Laboratory analysis (Direct shear) (IS: 2720-Part 13- 1986)		
Friction angle, $\phi$			

Landslide	Material type	Material depth <sup>1</sup> , m	Friction coefficient <sup>2</sup>	Turbulence coefficient <sup>3</sup> , m/sec <sup>2</sup>
Akpa (S.N. 5)	Gravelly sand	5	$\mu = 0.05, 0.1, 0.3$	$\xi = 100, 200, 300$
Baren Dogri (S.N. 7)	Gravelly sand	1.25	$\mu = 0.05, 0.1, 0.4$	$\xi = 100, 200, 300$
Pawari (S.N. 14)	Gravelly sand	1.25	$\mu = 0.05, 0.1, 0.4$	$\xi = 100, 200, 300$
Telangri (S.N. 15)	Gravelly sand	6.25	$\mu = 0.05, 0.1, 0.4$	$\xi = 100, 200, 300$
Urni (S.N. 19)	Gravelly sand	2.5	$\mu = 0.06, 0.1, 0.4$	$\xi = 100, 200, 300$

<sup>1</sup> Considering that fact that during slope failure, irrespective of type of trigger, entire loose material might not slide down, the depth is taken as only  $\frac{1}{4}$  (thickness) in the calculation. <sup>2</sup> Since the angle of run-out track (slope and river channel) varied a little beyond the suggested range  $2.8^\circ - 21.8^\circ$  or  $\mu = 0.05-0.4$  (Hung et al., 1984; RAMMS v.1.7.0), we kept out input in this suggested range wherever possible to avoid simulation uncertainty. <sup>3</sup> This range is used in view of the type of loose material i.e., granular in this study (RAMMS v.1.7.0).

**Table 4** Details of input parameters for run-out analysis. S.N. refers to serial number of landslides in Fig. 1.

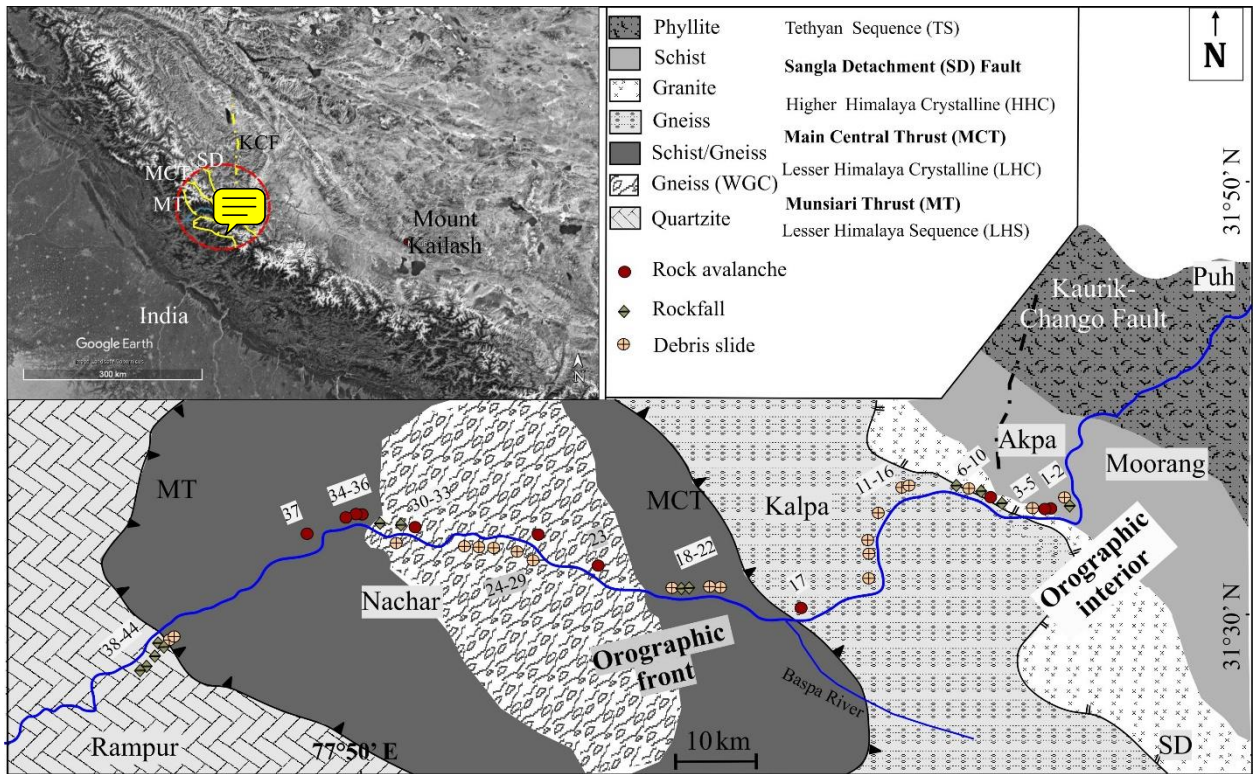


**Fig. 1** Geological setting. WGC: Wangtu Gneissic Complex. The red dashed circle in the inset represents the region within 100 km radius from the Satluj River (marked as blue line) that was used to determine the earthquake distribution in the area. KCF in inset refers to Kaurik-Chango Fault. The numbers 1-44 refer to serial number of landslides in Table 1.

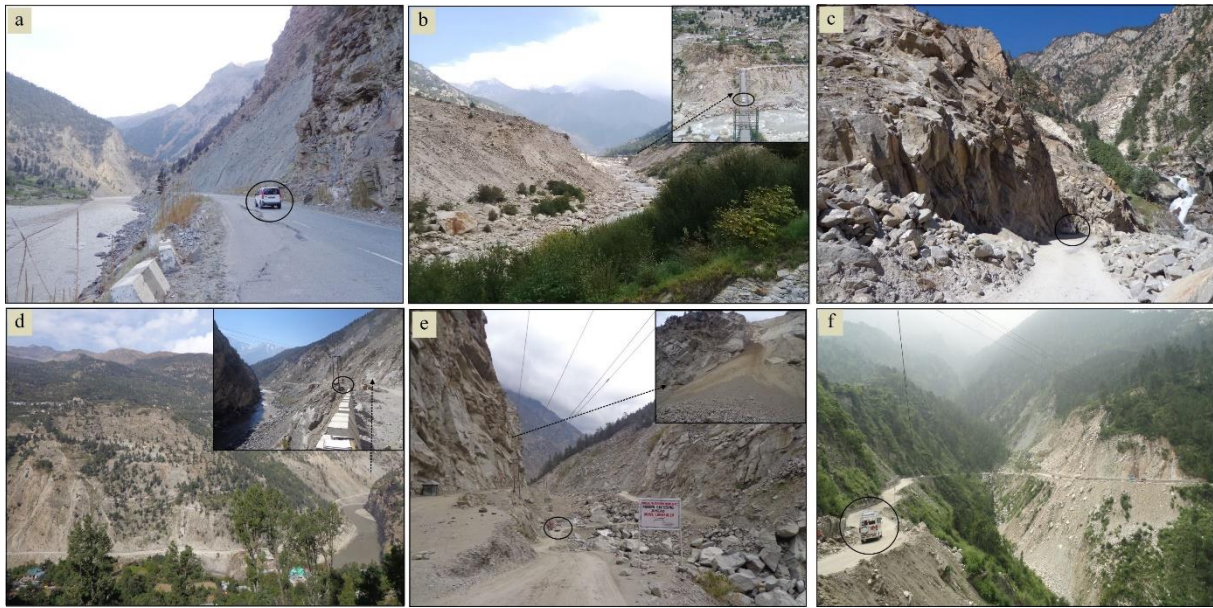


**Fig. 2** Field photographs of some of the landslides (a) Khokpa landslide (S.N.1); (b) Akpa\_III landslide (S.N. 5); (c) Rarang landslide (S.N. 6); (d) Pawari landslide (S.N.14); (e) Urni landslide (S.N.19); (f) Barauni Gad\_I\_S landslide (S.N. 38). Black circle in the pictures that encircles the vehicle is intended to represent the relative scale.

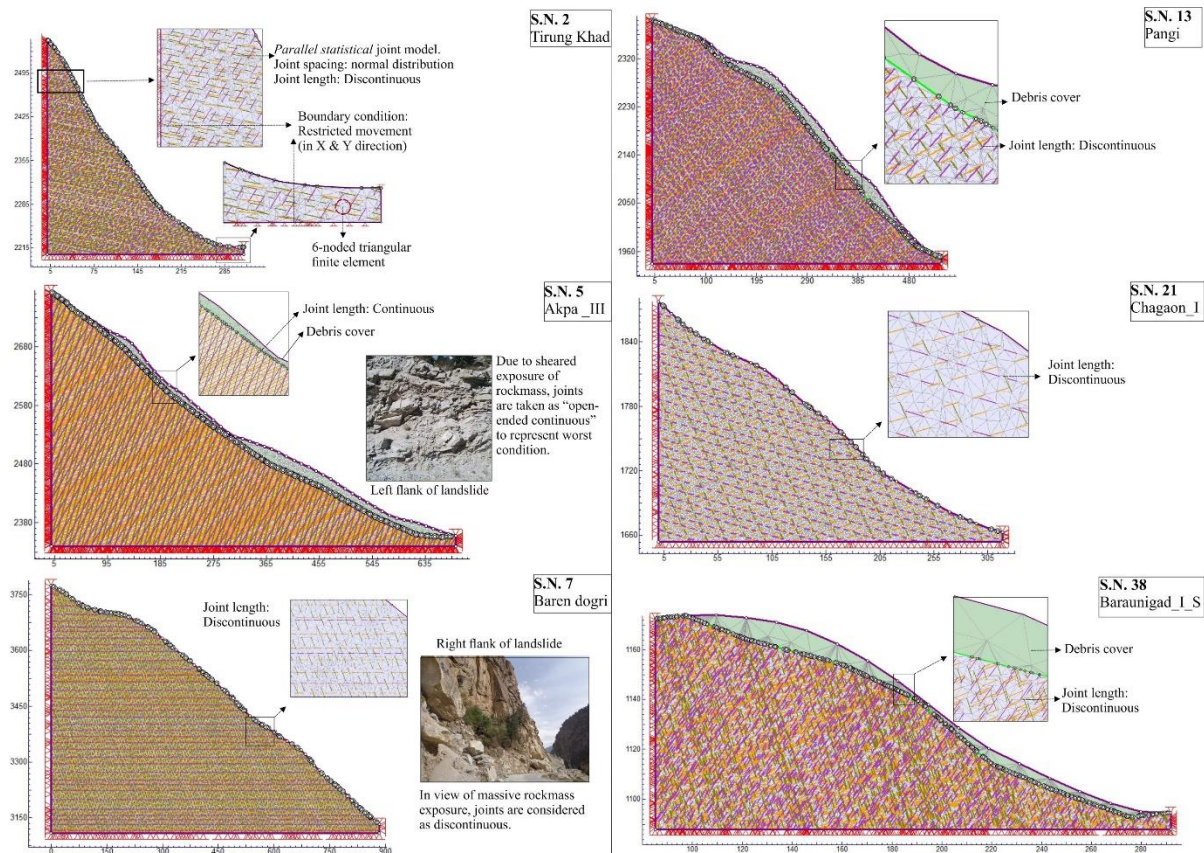


**Fig. 3** The FEM configuration of some of the slope models. S.N. refers to the serial no. of landslides in Table 1. The joint distribution in all the slopes was parallel-statistical with the normal distribution of joint spacing.

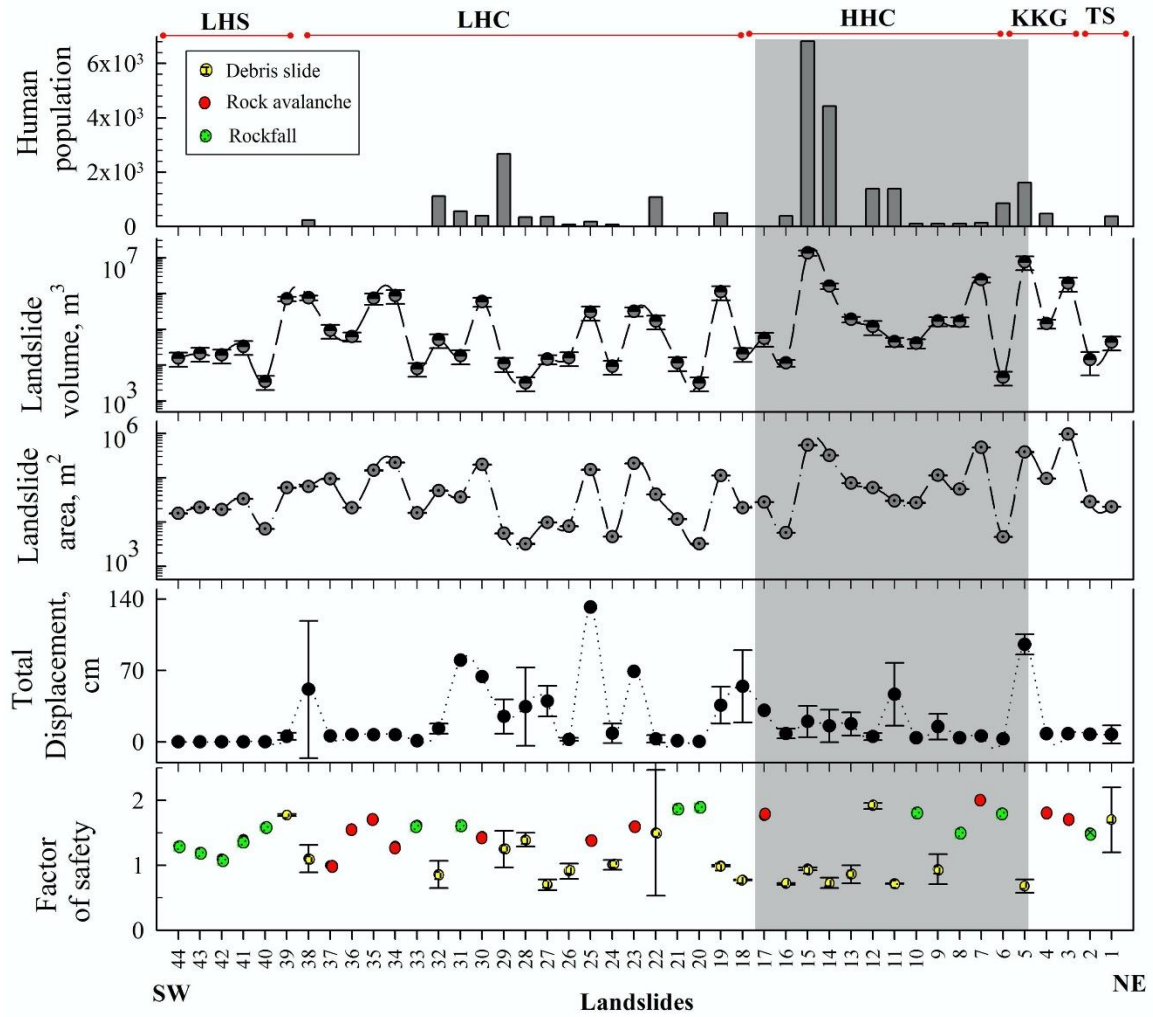


**Fig. 4** The FEM analysis of all forty-four landslides. Grey bar in the background highlights the Higher Himalaya Crystalline (HHC) region that comprises relatively more unstable landslides, ~~relatively more~~ landslide volume and human population. ~~Source of human population: Census 2011 (Govt. of India, New Delhi).~~ TS, KKG, HHC, LHC and LHS are Tethyan Sequence, Kinnaur Kailash Granite, Higher Himalaya Crystalline, Lesser Himalaya Crystalline and Lesser Himalaya Sequence, respectively

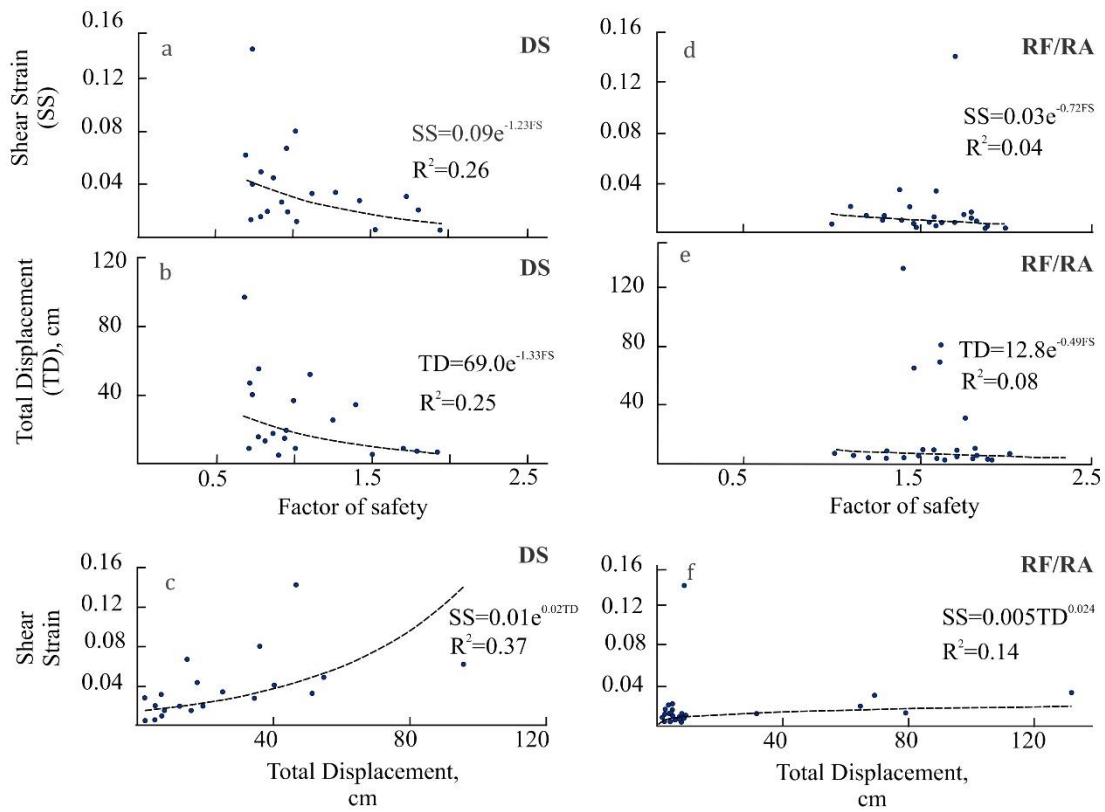


**Fig. 5** Relationship of Factor of Safety (FS), Total Displacement (TD) and Shear Strain (SS).  
 DS, RF, and RA refer to Debris slide, rock fall and rock avalanche, respectively.

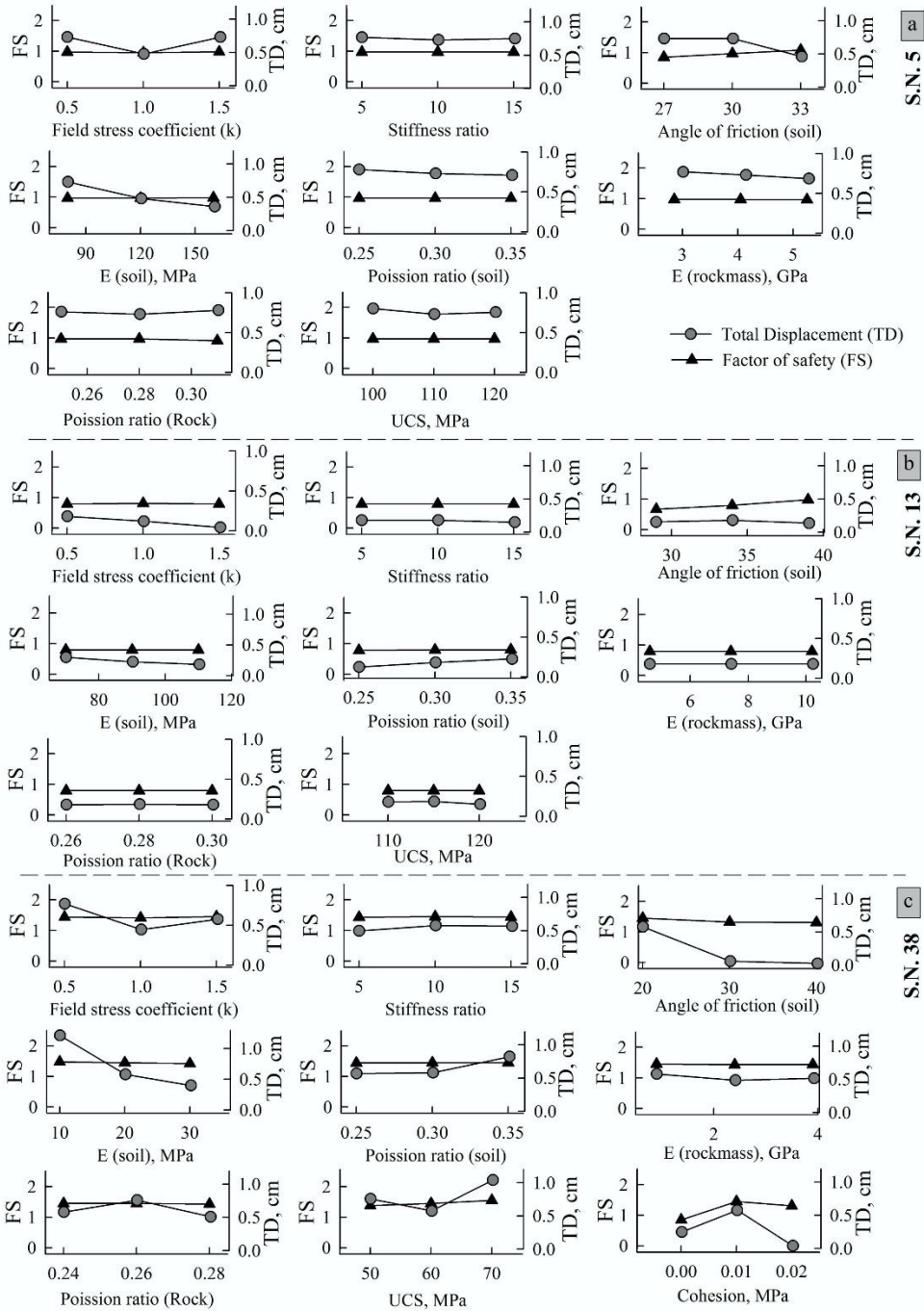


**Fig. 6** Parametric analysis of debris slides. (a) Akpa\_III (S.N. 5); (b) Pangi\_III (S.N. 13); (c) Barauni Gad\_I\_S (S.N. 38). S. N. refers to the serial no. of landslides in Table 1.

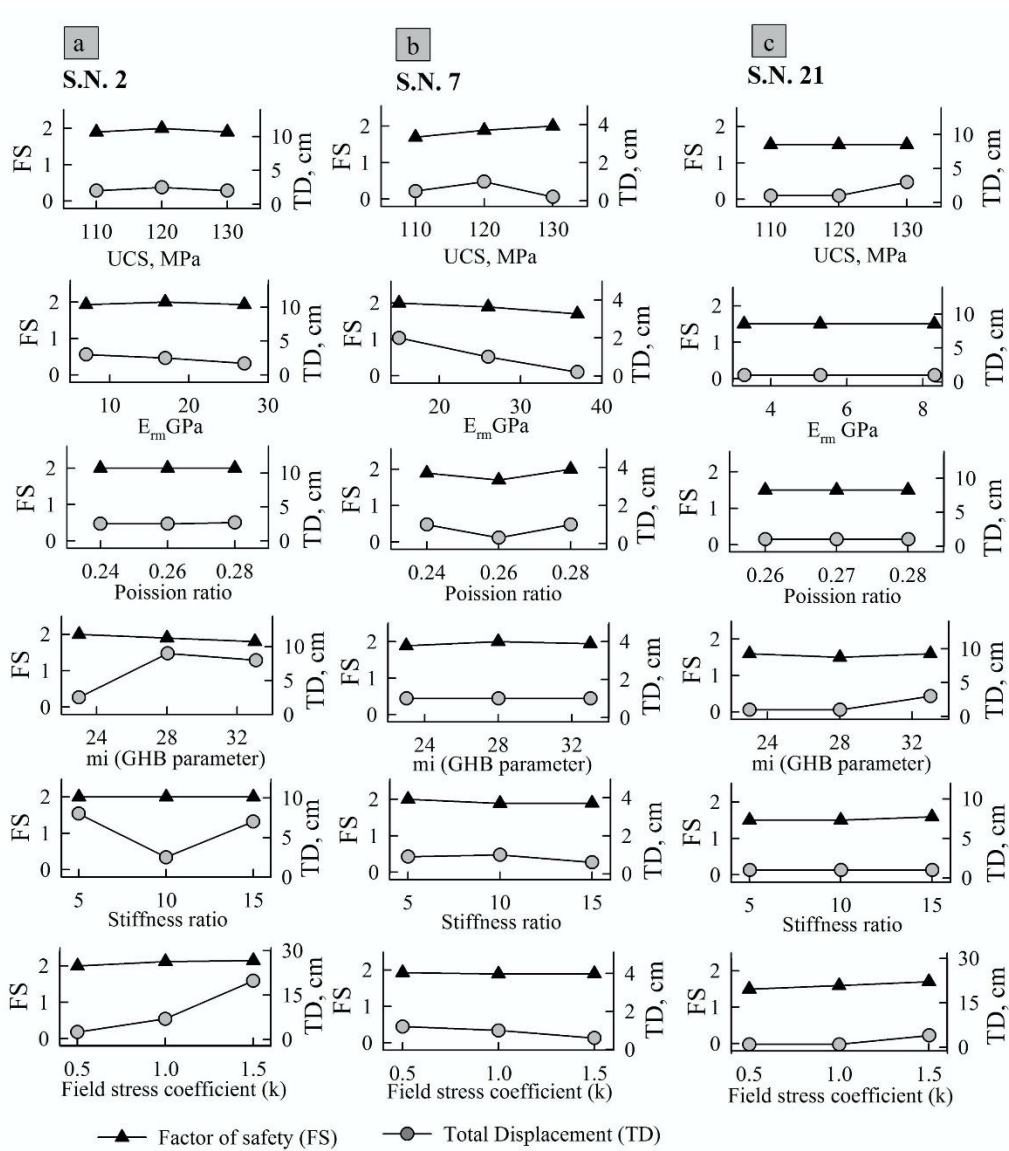


**Fig. 7** Parametric analysis of rockfall/rock avalanche. (a) Tirung khad (S.N. 2); (b) Baren Dogri (S.No. 7); (c) Chagaon\_II (S.N. 21).

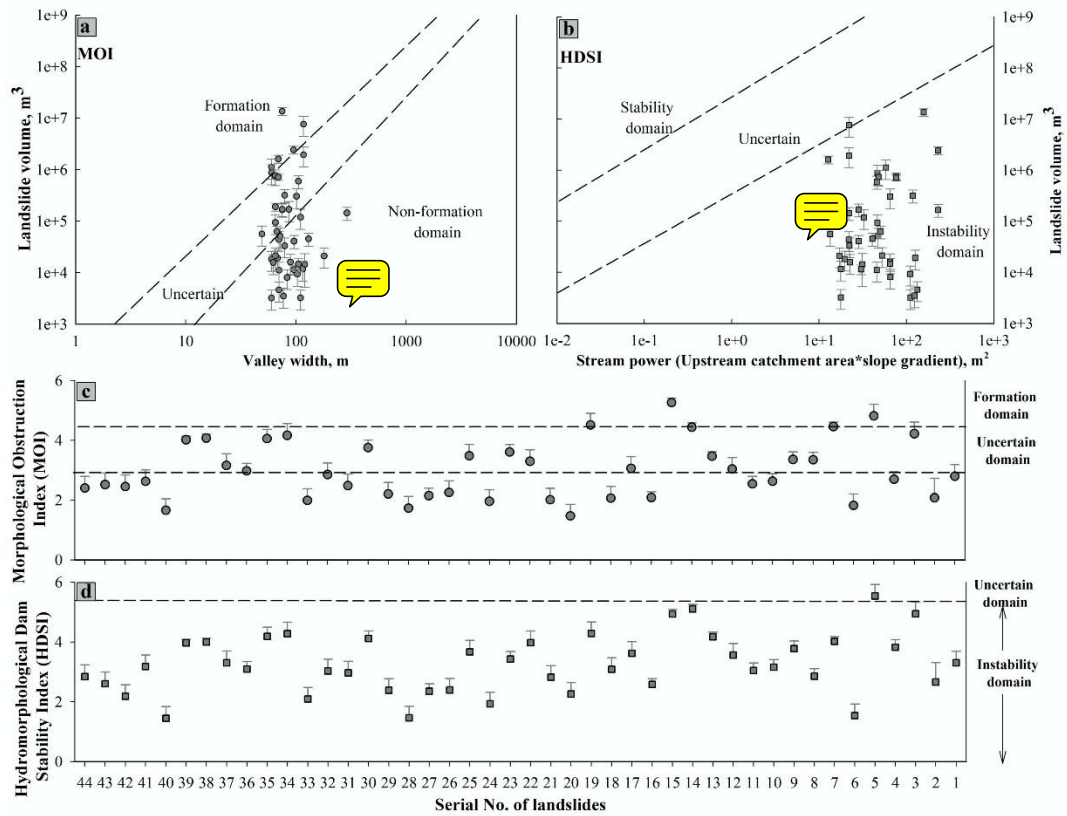


**Fig. 8** Landslide damming indices (a) Morphological Obstruction Index (MOI); (b) Hydro-morphological dam stability index (HDSI); (c) Landslides vs. MOI; (d) Landslides vs. HDSI.

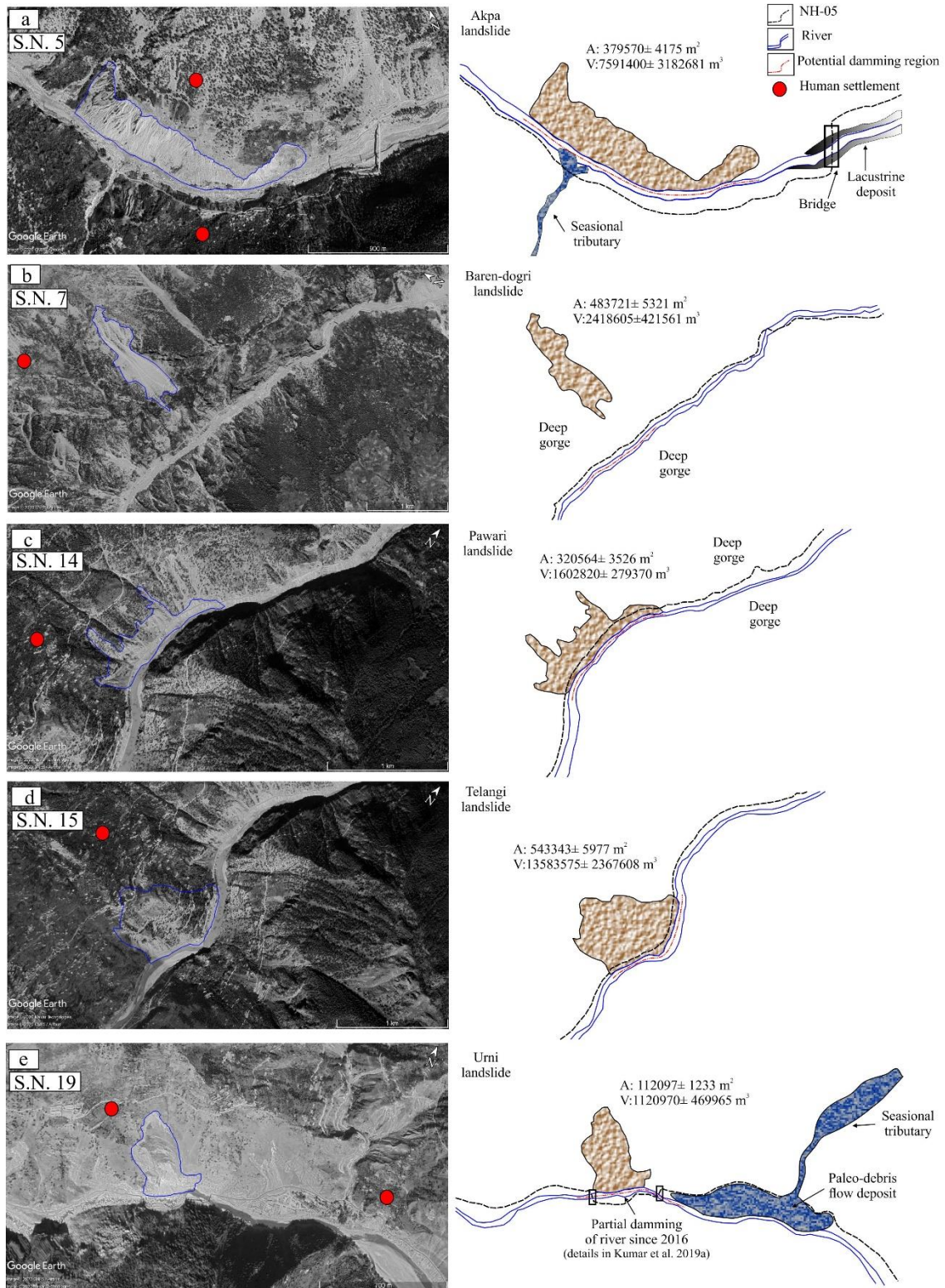


**Fig. 9** Potential landslide damming locations. (a) Akpa\_III landslide; (b) Baren dogri landslide; (c) Pawari landslide; (d) Telangi landslide; (e) Urni landslide. 



**Fig. 10** Field signatures of the landslide damming near Akpa\_III landslide. (a) Upstream view of Akpa landslide with lacustrine deposit at the left bank; (b) enlarged view of the lacustrine deposit with an arrow indicating the lacustrine sequence; (c) alternating fine-coarse sediments. F and C refer to fine (covered by yellow dashed lines) and coarse (covered by green dashed lines) sediments, respectively.

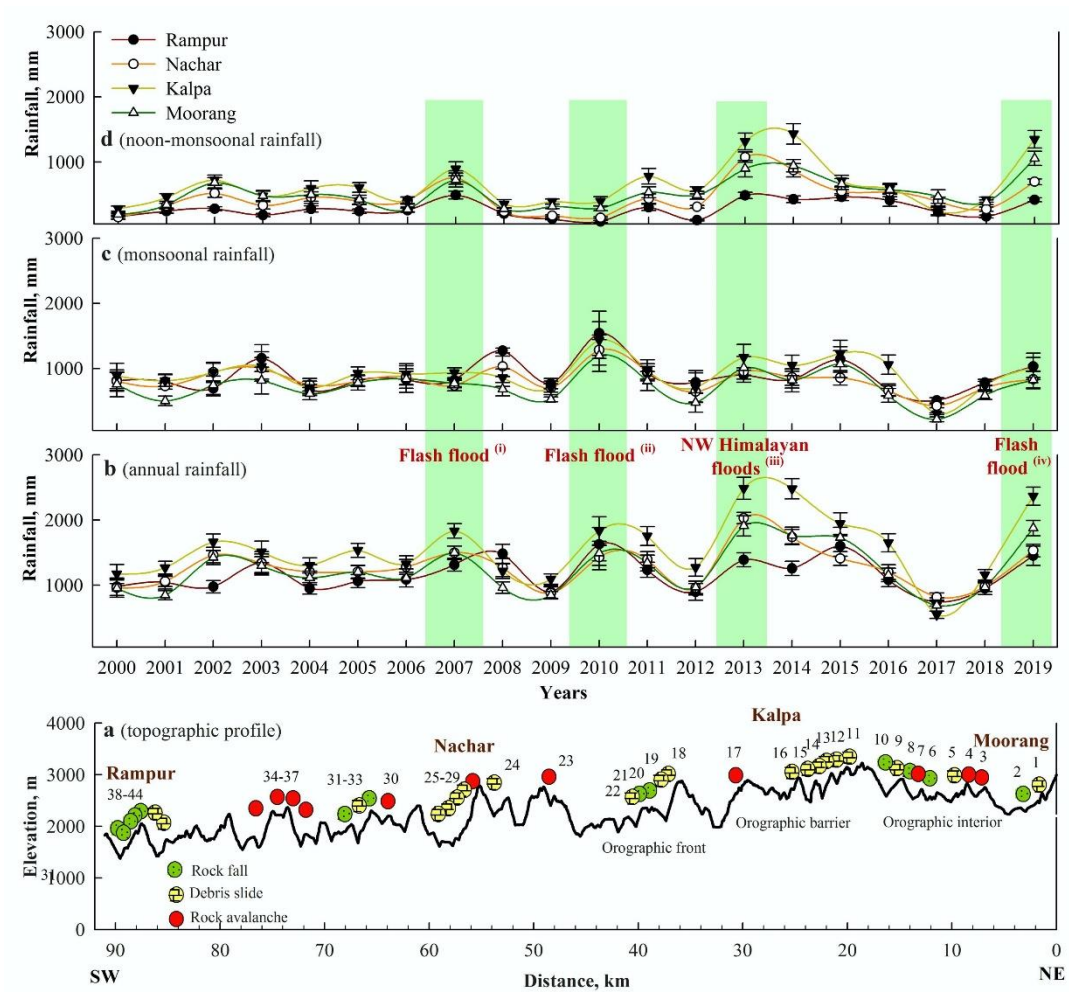


**Fig. 11** Rainfall distribution. (a) Topographic profile; (b) annual rainfall; (c) monsoonal (June-Sep.) rainfall; (d) non-monsoonal (Oct.-May) rainfall. Green bars represent the years of relatively more rainfall resulting into the flash floods, landslides and socio-economic loss in the region. (i):[hpenvs.nic.in](http://hpenvs.nic.in), retrieved on March 1, 2020; Department of Revenue, Govt. of H.P. (ii): [hpenvs.nic.in](http://hpenvs.nic.in), retrieved on March 1, 2020.(iii): Kumar et al., 2019a;[ndma.gov.in](http://ndma.gov.in), retrieved on march 1, 2020 (iv):[sandrp.in](http://sandrp.in), retrieved on march 1, 2020.The numbers 1-44 refer to serial number of the landslides.

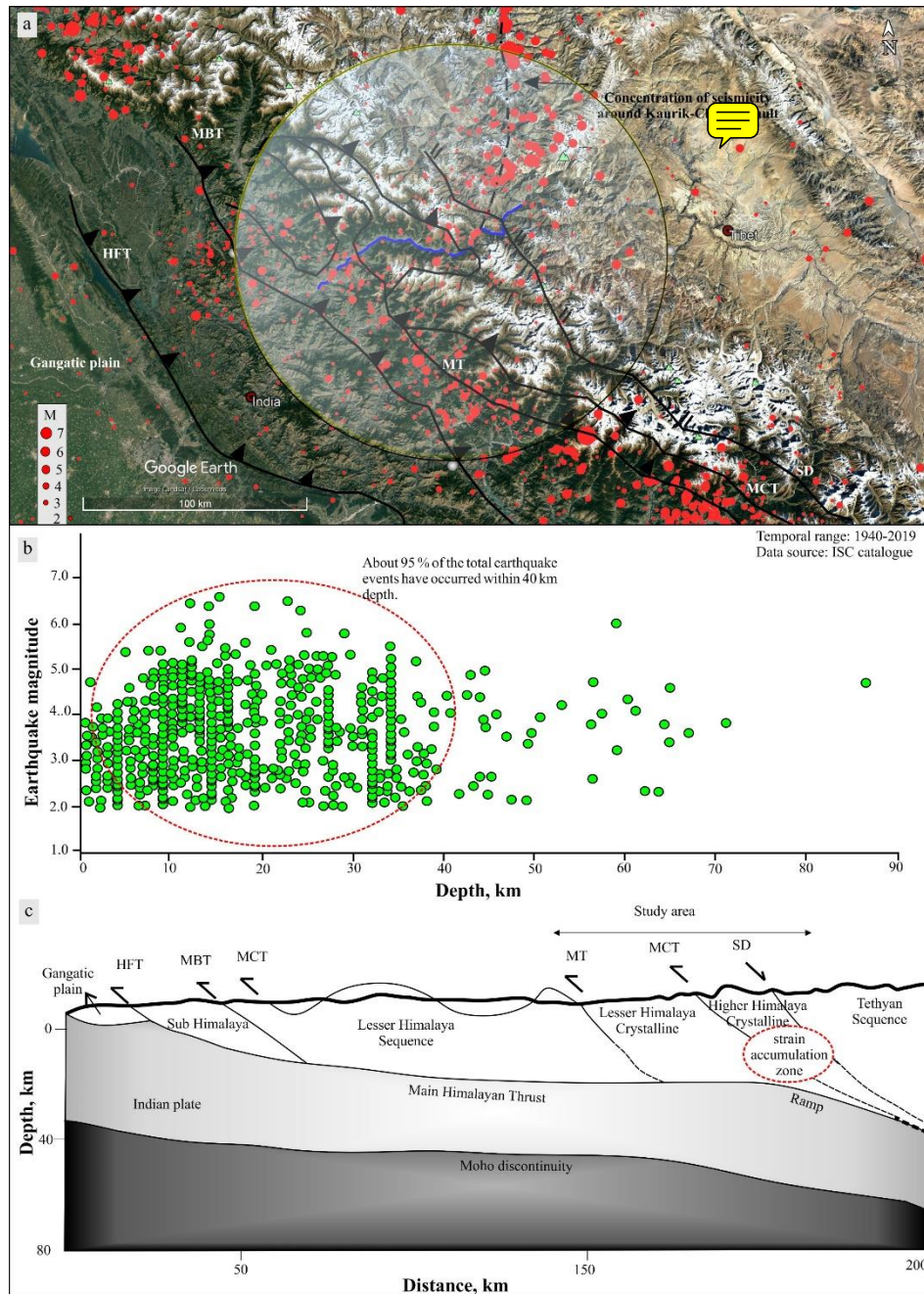


**Fig. 12** Earthquake distribution. (a) Spatial variation of earthquakes. The transparent circle represents the region within 100 km radius from the Satluj River (blue line). The black dashed line represents the seismic dominance around the Kaurik-Chango fault; (b) earthquake magnitude vs. focal depth. The red dashed region highlights the concentration of earthquakes within 40 km depth; (c) Cross section view (Based on Hazarika et al. 2017; Bilham, 2019). Red dashed circle represents the zone of strain accumulation caused by the Indian and Eurasian plate collision (Bilham, 2019). ISC: International Seismological Centre. HFT: Himalayan Frontal Thrust.

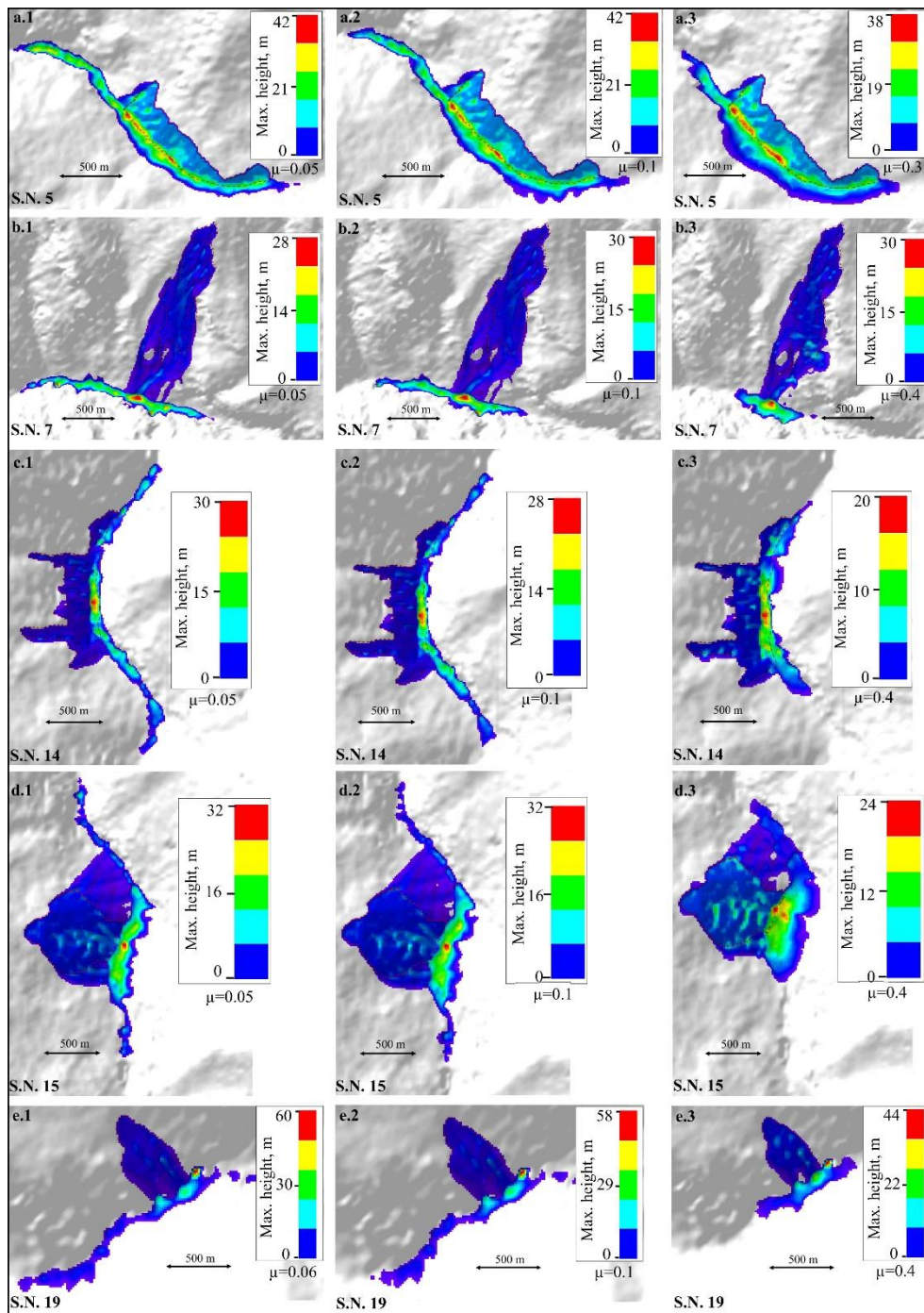


**Fig. 13** Results of the run-out analysis.  $\mu$  refers to coefficient of friction.

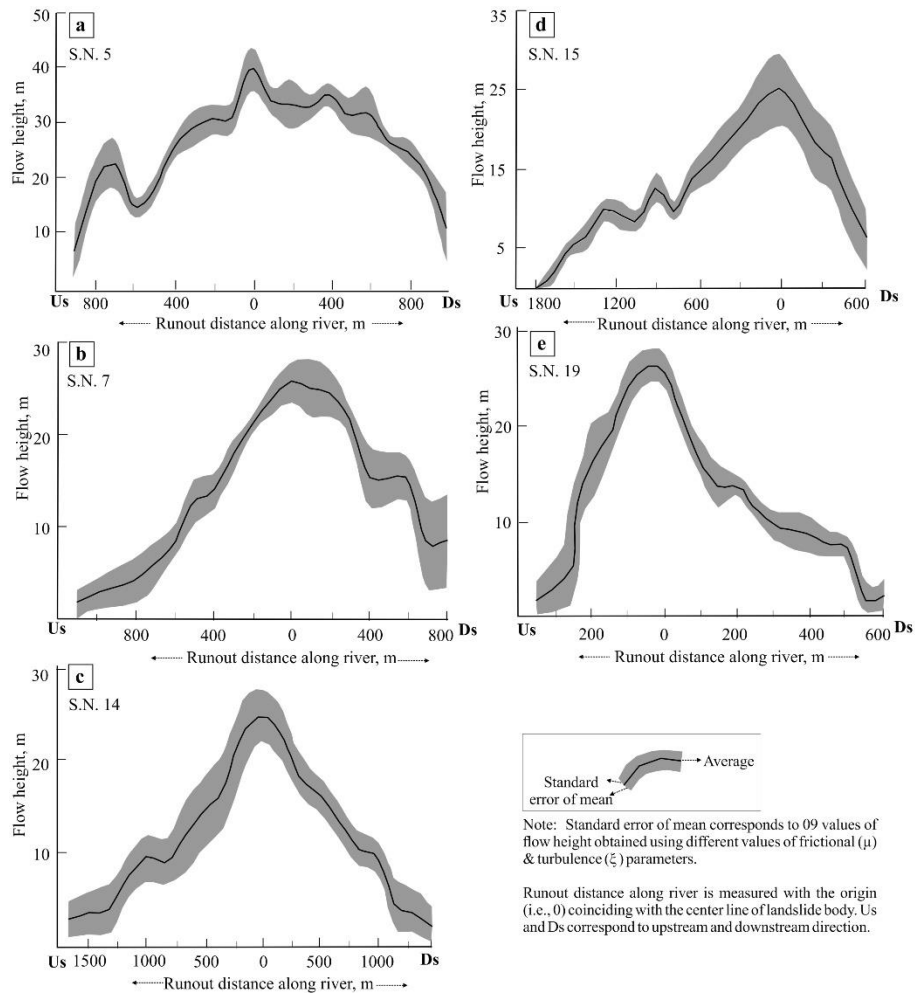


**Fig. 14** Results of run-out analysis at different values of  $\mu$  and  $\xi$ .  $\mu$  and  $\xi$  refer to coefficient of friction and turbulence, respectively.